LOCALIZED SIGNAL SUPPRESSION IN MAGNETIC PARTICLE IMAGING

A THESIS SUBMITTED TO
THE GRADUATE SCHOOL OF ENGINEERING AND SCIENCE
OF BILKENT UNIVERSITY
IN PARTIAL FULFILLMENT OF THE REQUIREMENTS FOR
THE DEGREE OF
MASTER OF SCIENCE
IN
ELECTRICAL AND ELECTRONICS ENGINEERING

By
Ege Kor
August 2025

Localized Signal Suppression in Magnetic Particle Imaging
By Ege Kor
August 2025

We certify that we have read this thesis and that in our opinion it is fully adequate, in scope and in quality, as a thesis for the degree of Master of Science.

Emine Ülkü Sarıtaş Çukur(Advisor)

Ergin Atalar

Yusuf Ziya İder

Approved for the Graduate School of Engineering and Science:

Orhan Arıkan
Director of the Graduate School

ABSTRACT

LOCALIZED SIGNAL SUPPRESSION IN MAGNETIC PARTICLE IMAGING

Ege Kor
M.S. in Electrical and Electronics Engineering
Advisor: Emine Ülkü Sarıtaş Çukur
August 2025

Magnetic Particle Imaging (MPI) is a tracer-based imaging modality offering high temporal and spatial resolution without any signal from the background tissue. MPI images the spatial distribution of magnetic nanoparticles (MNPs). However, these MNPs can accumulate in off-target organs, such as the liver and spleen, and the resulting strong signal can obscure nearby target signals. This problem is further exacerbated by the broad point spread function of the imaging system, which causes even distant off-target regions to interfere with the desired signal. This thesis proposes localized signal suppression through the use of additional DC saturation fields that locally saturate MNP magnetization. After deriving the relevant imaging equations, the requirements for the saturation field strength are determined via simulations. Next, several coil designs are evaluated for localized MNP saturation. Quantitative results show that there is a balance between suppression efficiency and spatial spillover, guiding optimal coil design. Electromagnetic interference caused by interactions between the saturation coil and the rest of the MPI hardware is investigated by analyzing the sources of secondary field inductions. Among several potential solutions to address this challenge, an L-choke component is incorporated into the final circuitry to minimize interference. Imaging experiments on a custom MPI scanner demonstrate that the proposed approach effectively reduces off-target signals and enhances target-to-background contrast in MPI images. The results of this thesis demonstrate localized signal suppression as a viable and successful approach for improving contrast in MPI in the case of MNP accumulation in off-target tissues.

Keywords: Magnetic particle imaging (MPI), signal suppression, saturation field, interference, induction, coil design.

ÖZET

MANYETİK PARÇACIK GÖRÜNTÜLEMEDE YEREL SİNYAL BASTIRMA

Ege Kor
Elektrik ve Elektronik Mühendisliği, Yüksek Lisans
Tez Danışmanı: Emine Ülkü Sarıtaş Çukur
Ağustos 2025

Manyetik Parçacık Görüntüleme (MPG), arka plan dokusundan herhangi bir sinyal olmaksızın yüksek zamansal ve mekansal çözünürlük sunan, izleyici madde tabanlı bir görüntüleme yöntemidir. MPG, manyetik nanoparçacıkların (MNP'ler) uzamsal dağılımını görüntüler. Ancak MNP'ler, karaciğer ve dalak gibi hedef dışı organlarda birikebilir ve ortaya çıkan güçlü sinyal, yakındaki hedef sinyalleri belirsizleştirebilir. Görüntüleme sisteminin geniş noktasal yayılma fonksiyonu bu problemi daha da kötüleştirir; çünkü uzaktaki hedef dışı bölgeler bile istenen sinyalle girişime neden olabilir. Bu tez, MNP manyetizasyonunu yerel olarak doygunluğa ulaştıran doğru akım (DC) doygunluk alanlarının kullanımıyla yerel olarak sinyal bastırılmasını önermektedir. İlgili görüntüleme denklemleri çıkarıldıktan sonra, doygunluk alanı şiddetine yönelik gereksinimler benzetimlerle belirlenmiştir. Daha sonra, yerel MNP doygunluğu için çeşitli bobin tasarımları değerlendirilmiştir. Nicel sonuçlar, bastırma verimliliği ile uzamsal yayılma arasında bir denge olduğunu göstermekte ve bu da en uygun bobin tasarımını yönlendirmektedir. Doygunluk bobini ile MPG donanımının geri kalanı arasındaki etkileşimlerden kaynaklanan elektromanyetik girişim, ikincil alan indüksiyonlarının kaynakları analiz edilerek incelenmiştir. Bu sorunu çözmek amacıyla öne sürülen çeşitli çözümler arasında, indüksiyon sinyalini en aza indirmek için devreye bir boğucu bobin (L-choke) bileşeni entegre edilmiştir. Özel olarak tasarlanmış bir MPG tarayıcısında yapılan görüntüleme deneyleri, önerilen yaklaşımın hedef dışı sinyalleri etkin bir şekilde azalttığını ve MPG görüntülerinde hedef ve arka plan arasındaki kontrastı artırdığını göstermektedir. Bu tez çalışmasının sonuçları, MNP birikiminin hedef dışı dokularda gerçekleştiği durumlarda MPG kontrastını iyileştirmek için yerel sinyal bastırmanın uygulanabilir ve başarılı bir yaklaşım olduğunu ortaya koymaktadır.

Anahtar sözcükler: Manyetik parçacık görüntüleme (MPG), sinyal bastırma, doygunluk alanı, girişim, indüksiyon, bobin tasarımı.

Acknowledgement

My interest in medical imaging stems from a deep desire to contribute to healthcare through technology. The potential of imaging techniques to improve diagnosis and treatment motivates me to pursue advanced research in this field, combining my passion for engineering and medicine to make a meaningful impact on human health.

First and foremost, I would like to express my sincere gratitude to my advisor, Assoc. Prof. Emine Ülkü Sarıtaş. Throughout my graduate studies, I have learned a great deal from her expertise, guidance, and encouragement. Her dedication to science and her students has been truly inspiring, and I feel privileged to have been under her mentorship. Her support has been instrumental in shaping both my academic skills and my approach to research.

I would also like to thank Prof. Ergin Atalar and Prof. Yusuf Ziya İder for their valuable time and effort as members of my thesis committee. Their insightful feedback and constructive comments were greatly appreciated and contributed significantly to the improvement of my work.

I am also deeply thankful to Dr. Musa Tunç Arslan, who patiently taught me the practical aspects of experimental work in the laboratory. His assistance during my initial days in the lab helped me gain confidence and develop hands-on skills essential for my research.

My heartfelt thanks go to my family, who have continuously encouraged me throughout this journey. Their unwavering moral and financial support motivated me to overcome difficulties and pursue my academic goals with determination. I am forever grateful for their love and belief in me.

I would also like to acknowledge Bilkent University for providing me with an exceptional academic environment and a unique vision. The opportunities and intellectual atmosphere here have greatly contributed to my personal and

professional growth.

I would like to thank the Scientific and Technological Research Council of Turkey (TUBITAK Grant No: 122E162, 120E208, 22AG016/23AG005) for supporting the work in this thesis.

Finally, I extend my appreciation to the entire UMRAM research group. Being part of such a supportive and enthusiastic team has made this experience enjoyable and rewarding. Their collaboration and friendship have been invaluable throughout my studies.

Ultimately, this journey has brought me ever closer to realizing my aspirations and making a lasting impact in my field.

Ege Kor
August 2025

Contents

List of Figures

List of Tables

Chapter 1

Introduction

Magnetic Particle Imaging (MPI) is an emerging tomographic imaging modality that visualizes the spatial distribution of magnetic nanoparticles (MNPs) by leveraging their strongly non-linear magnetization response under oscillating magnetic fields [1, 2]. Since its initial demonstration by Gleich and Weizenecker in 2005 [1], MPI has garnered attention for its unique ability to directly and quantitatively image MNPs with high sensitivity and temporal resolution, while avoiding the use of ionizing radiation [2, 3]. This makes MPI highly suitable for various clinical and preclinical applications, including but not limited to angiographic studies [4], stem cell monitoring [5, 6], inflammation mapping [7, 8], image-guided therapy [9, 10], brain trauma detection [11], oncology imaging [12], and localized hyperthermia treatments [13].

While the sensitivity of MPI in detecting MNPs is a key strength, it can also lead to challenges. When MNPs accumulate in certain off-target organs in high concentrations, they can produce overwhelming signal levels that obscure weaker signals from nearby tissues or pathologies [3, 14]. This disproportionate signal distribution can compromise image clarity and reduce the diagnostic reliability of MPI scans. This problem can be further exacerbated by the relatively wide point spread function of the imaging system, causing even distant off-target regions to interfere with the desired signal.

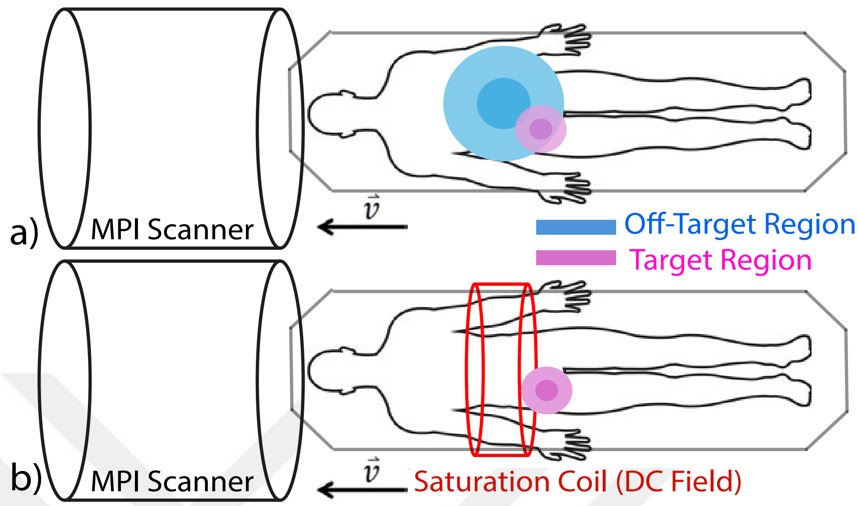

Figure 1.1: Conceptual illustration of selective signal suppression using a saturation coil in MPI. (a) Without a saturation field, the strong signal from an off-target region (e.g., liver) overpowers the weaker signal from the target region (e.g., vessel), making it difficult to detect. (b) By applying a local DC magnetic field using a saturation coil, the signal from the off-target region can be suppressed, allowing clear detection of the low-amplitude signal from the target region.

The biodistribution of MNPs is inherently non-uniform, governed by systemic and cellular mechanisms, as well as nanoparticle-specific attributes like size, coating, and charge [3, 15]. Tissues associated with the mononuclear phagocyte system, such as the liver and spleen, are known for their ability to uptake substantial amounts of MNPs, whereas nearby vasculature or pathological tissues may exhibit minimal accumulation [4, 14]. This imbalance poses a significant barrier to acquiring consistent image quality near an off-target high-accumulation region.

To mitigate this limitation, this thesis proposes a strategy involving localized magnetic saturation, in which a strong DC magnetic field is applied to off-target regions with excessive MNP accumulation. This technique renders MNPs in these regions magnetically saturated, thereby suppressing their contribution to the time-varying MPI signal during image acquisition, as depicted in Fig.1.1.

In this thesis, first, the theory of signal suppression via the use of a saturation field is proposed. The magnetic field required for sufficient signal suppression is investigated via simulations and numerical evaluations. Next, several saturation coil designs are implemented and evaluated, with the goal of saturation MNP magnetization in specific regions without adversely affecting those within the targeted field-of-view (FOV).

Our custom-built MPI system is used for experimental validation of the proposed approach. During the integration of a saturation coil into an MPI scanner, an important challenge is the generation of unintended electromagnetic interference, resulting from the interaction between the saturation coil and the rest of the MPI hardware. In this thesis, this interference is referred to as the "secondary field induction", a phenomenon governed by Faraday's law. Alternative solutions to address this challenge are investigated, and an L-choke component is incorporated into the overall circuitry to effectively overcome this interference. Finally, a series of imaging experiments are performed to demonstrate localized signal suppression of dominant off-target signals through the use of saturation field, while improving the visibility of nearby target regions.

Chapter 2

Background and Theory

Magnetic Particle Imaging (MPI) is a tracer-based imaging modality that maps the spatial distribution and concentration of magnetic nanoparticles (MNPs), such as superparamagnetic iron oxide nanoparticles (SPIOs), by leveraging their nonlinear magnetization response to external magnetic fields [1, 16, 17]. Unlike conventional tracer-based imaging modalities such as positron emission tomography (PET), MPI does not utilize radioactive tracers or rely on ionizing radiation, and already offers higher spatial resolution. Furthermore, due to lack of background signal from biological tissue, MPI offers high sensitivity for detecting MNPs.

2.1 Magnetization Behavior of Nanoparticles

As outlined in Fig. 2.1, the magnetization response of MNPs to an applied magnetic field H is nonlinear and is governed by the Langevin function. In the dynamic region, as H increases, the MNP magnetization $M(H)$ rises sharply. However, beyond a certain field threshold, the magnetization enters the saturation regime, where further increases in H yield negligible changes in $M(H)$. This phenomenon enables selective signal generation from MNPs with unsaturated

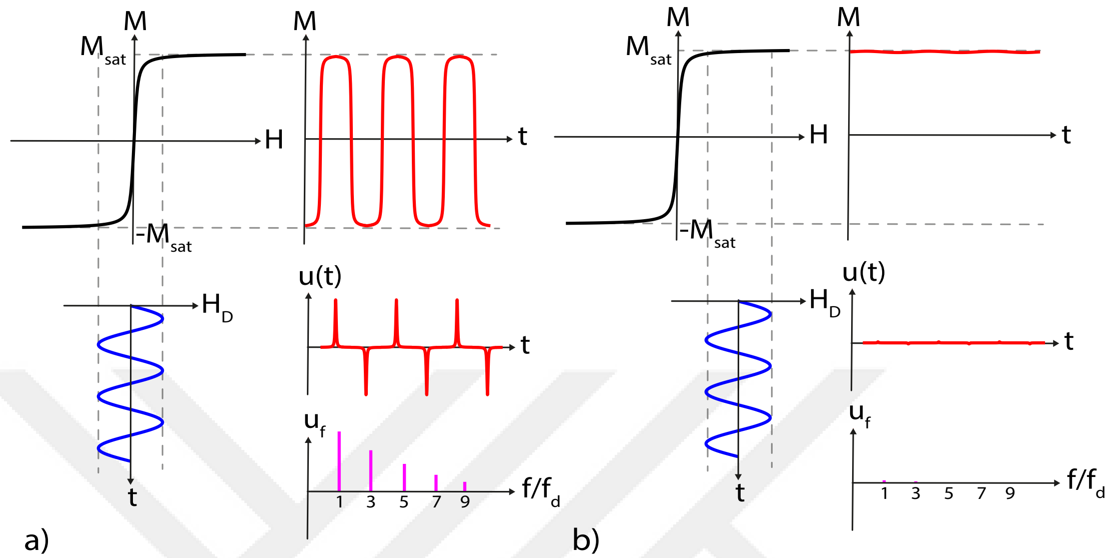

Figure 2.1: (a) **Dynamic Region:** In this region, the applied magnetic field H has zero or a low DC level and the magnetic nanoparticle (MNP) magnetization is unsaturated. When an oscillating magnetic field called the drive field is applied with amplitude H_D, the MNP magnetization M is highly responsive and varies non-linearly with H. This causes a time-varying magnetization $M(t)$, shown with the periodic switching in the red curve (top right). This time-varying magnetization induces a time-varying voltage $u(t)$ in the receive coil (middle right), producing strong signal components at the odd harmonics of the applied drive field frequency f_d (bottom right). (b) **Saturation Region:** Here, the external magnetic field has a DC component that is strong enough to saturate the MNP magnetization, keeping their magnetization M nearly constant at the maximum M_{sat}. Thus, despite the applied drive field, the magnetization shows negligible variation as a function of time (top right), resulting in a weak induced signal $u(t)$ (middle right) and a nearly zero frequency spectrum (bottom right).

magnetization, forming the core principle of MPI spatial encoding.

The net magnetization of an ensemble of MNPs is given by [1, 16, 17]:

$$M(H) = cm\mathcal{L}(kH) = cm\left(\coth(kH) - \frac{1}{kH}\right), \tag{2.1}$$

where

$$k = \frac{\mu_0 m}{k_B T}. \tag{2.2}$$

Here, c is the MNP density (particles/m^3), m is the magnetic moment of a single nanoparticle, μ_0 is the vacuum permeability, k_B is the Boltzmann's constant, and T is the absolute temperature. For spherical single-domain nanoparticles with core diameter d, the magnetic moment can be approximated as [16]:

$$m = \frac{M_{\text{sat}} \pi d^3}{6} \tag{2.3}$$

Here, M_{sat} is the saturation magnetization of the nanoparticle material. As the diameter of MNPs increases, the magnetic field strength needed to saturate the MNP decreases, which enables improved spatial resolution in MPI. However, there exists an upper limit to this trend, as the relaxation effect becomes significant for MNPs above a certain diameter. The relaxation effects refer to the time-dependent delay in the MNP response to external field variations, which can adversely impact imaging performance when the particle size becomes excessively large [17].

2.2 Magnetic Particle Imaging

A typical MPI system incorporates three primary magnetic field components to image the spatial distribution of MNPs. First, a selection field (SF) is applied to define a specific spatial point known as the field-free region (FFR), where the system can detect the presence of MNPs. Second, a sinusoidal drive field (DF) with sufficient amplitude is used to excite the MNPs and cause a time-varying magnetization response of MNPs located near the FFR. Third, a gradually changing focus field (FF) is employed to shift the FFR throughout the imaging volume, thereby expanding the field-of-view (FOV) beyond the range achievable by the DF alone [17]. The response of the MNPs to the time-varying magnetic fields is detected through inductive coupling by a receive coil. This induced signal carries information about the MNP concentration and its spatial distribution. By systematically moving the FFR across the imaging volume, a detailed map of the MNP distribution can be reconstructed from the received signal. Figure 2.2 illustrates typical MPI scanner topologies.

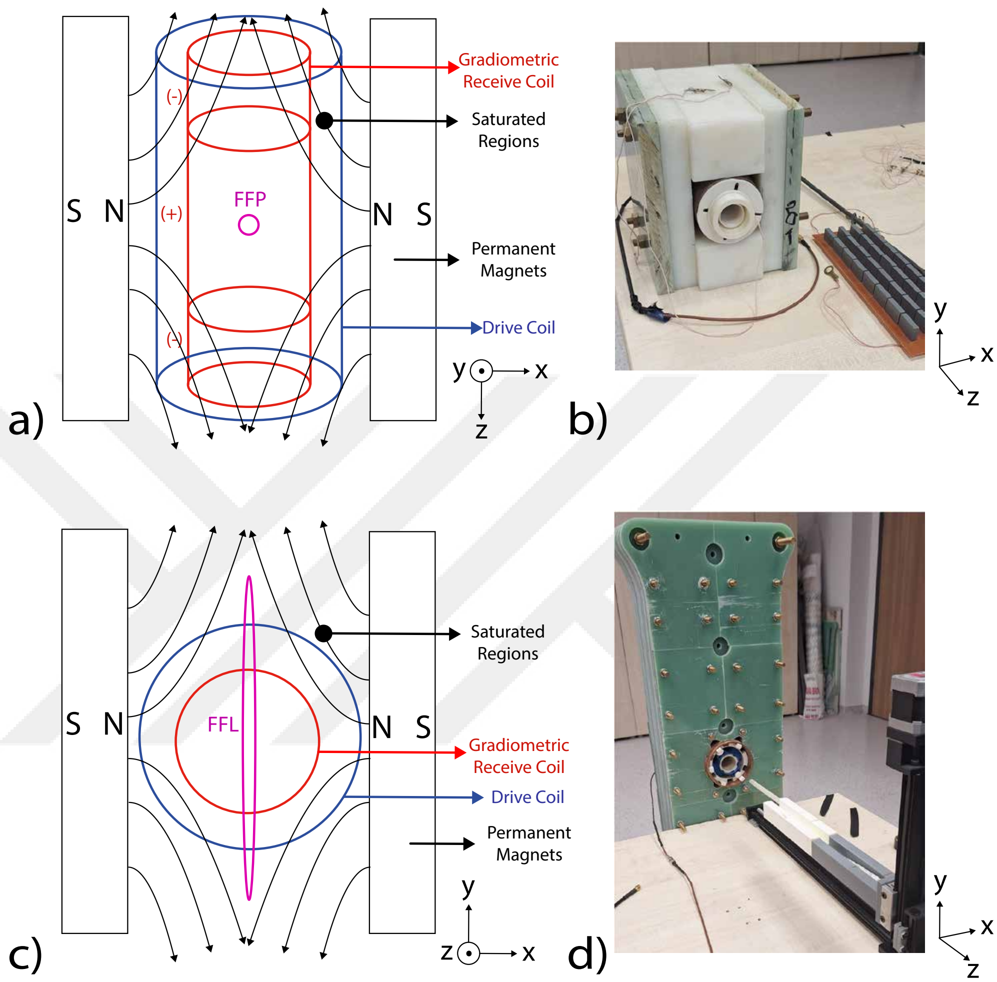

Figure 2.2: Typical MPI scanner topologies. (a) A schematic of a MPI scanner where the field free region (FFR) is a field free point (FFP). Black lines represent the selection field (SF) generated by two opposing permanent magnets, which create a FFP at the center (see the magenta circle). MNPs near the FFP are excited by a time-varying drive field, and their response is detected inductively by the receive coil. Spatial encoding is achieved by the SF, which causes the MNPs outside the FFP to be saturated, such that only the MNPs near the FFP induce signal. (b) Our in-house FFP scanner system with 4.8 T/m SF gradient along the x-direction. (c) A schematic of a MPI scanner where the FFR is a field free line (FFL). The magenta ellipsoid marks the FFL region along a line. The MNP signal is acquired from the entire line, enabling projection-format imaging. (d) Our in-house FFL scanner system with FFL along the y-axis and 4.4 T/m SF gradients along the x- and z-directions.

2.2.1 Selection Field for Spatial Encoding

The SF in MPI provides spatial encoding by creating a static magnetic field gradient that defines a FFR, where the magnetic field strength approaches zero. In areas distant from the FFR, the magnetic field due to SF increases rapidly, causing the MNPs in those regions to become saturated. These saturated MNPs no longer respond to time-varying excitations, effectively silencing their contribution to the received signal. In contrast, only the MNPs near the FFR remain within their dynamic magnetization range and produce detectable signals in response to a time-varying magnetic field. This selective sensitivity forms the foundation of spatial encoding in MPI [17].

For the 1D case, the SF can be expressed as:

$$H_s(x) = -Gx \tag{2.4}$$

where G is the magnetic field gradient of the SF, $x = 0$ is the equilibrium FFR location, and the negative sign is introduced for convenience.

For the ideal 3D case, the SF can be expressed as:

$$\mathbf{H_s} = \mathbf{Gx} = G_x x + G_y y + G_z z \tag{2.5}$$

where

$$G_i = \frac{\partial}{\partial i} H_{s,i} \tag{2.6}$$

Here, $\mathbf{x}$ is position in space, $\mathbf{G}$ is the SF gradient matrix, and G_i denotes the gradient of the SF along the i-axis. Here, the gradient matrix is diagonal and satisfies the following condition:

$$G_x + G_y + G_z = 0 \tag{2.7}$$

For this 3D case, $\mathbf{x} = \mathbf{0}$ is the equilibrium FFR location, i.e., the isocenter of the MPI scanner.

2.2.2 Drive Field for MNP Excitation

In MPI, the DF is a time-varying magnetic field that is superimposed onto the static SF. Only MNPs located at or near the FFP remain unsaturated and thus can respond to the oscillatory DF by varying their magnetization over time. The resulting time-varying magnetization induces a voltage in the receive coil according to Faraday's law. The primary function of DF is to excite the MNPs and to cause the FFR to move along a chosen axis during signal acquisition. This movement allows the system to capture magnetization responses from the MNPs located across the trajectory of the FFR movement, rather than being restricted to a single point in space [1, 17].

In its most common form, the DF is a purely sinusoidal waveform:

$$H_d(t) = H_{\text{peak}} \cos(2\pi f_d t) \tag{2.8}$$

where H_{peak} represents the DF amplitude, and f_d is the DF frequency. The total magnetic field experienced by the MNPs can be written as the superposition of the SF and DF, i.e.,

$$H(x,t) = H_s(x) + H_d(t) = -Gx + H_{\text{peak}} \cos(2\pi f_d t) \tag{2.9}$$

The instantaneous position of the FFP, i.e., the position that satisfies $H(x,t) = 0$, can then be written as:

$$x_{\text{s}}(t) = \frac{H_d(t)}{G} = \frac{H_{\text{peak}}}{G} \cos(2\pi f_d t) \tag{2.10}$$

As seen in this relation, the spatial extent of the FOV covered by the FFR movement can be expressed as:

$$\left[-\frac{\text{FOV}}{2}, \frac{\text{FOV}}{2}\right] = \left[-\frac{H_{\text{peak}}}{G}, \frac{H_{\text{peak}}}{G}\right] \tag{2.11}$$

Accordingly, the FOV size is determined by both the DF amplitude and the SF gradient. As the FFR moves across the FOV, only the MNPs near its instantaneous location contribute to the received signal. The speed at which the FFR moves can be expressed as:

$$\dot{x}_{\mathrm{s}}(t) = \frac{dx_{\mathrm{s}}(t)}{dt} = -2\pi f_d \frac{H_{\mathrm{peak}}}{G} \sin(2\pi f_d t) \tag{2.12}$$

Hence, the FFR moves most rapidly at the center of the FOV and its speed goes down to zero near the the two ends of the FOV [17].

2.2.3 Focus Field for Extending FOV

Because the DF is limited in both amplitude due to hardware and safety constraints, it cannot independently provide full access to an extended FOV [3]. To extend the spatial coverage of MPI, a supplementary magnetic field known as the focus field (FF) is employed. This field, characterized by its high amplitude and low frequency, enables repositioning of the FFR to areas that are otherwise inaccessible using the DF alone [2, 18, 19].

2.2.4 Signal and Image Equations

Assuming a 1D MNP distribution and ideal conditions (i.e., neglecting the relaxation effects of the MNPs and assuming no coupling between the drive and receive coils), the signal detected by the receive coil can be expressed as [17]:

$$\begin{aligned} s(t) &= B_1 \frac{d}{dt} \int M(H(x,t))\, dx \qquad (2.13) \\ &= B_1 m \frac{d}{dt} \int \rho(x) \mathcal{L}(kH(x,t))\, dx \qquad (2.14) \end{aligned}$$

Here, $s(t)$ is the induced signal, B_1 is the receive coil sensitivity (assumed to be uniform in this equation) and $\rho(x)$ is the spatial distribution of MNP concentration.

Next, inserting Equation (2.10) into Equation (2.9), the total magnetic field can be expressed in terms of the instantaneous FFR position:

$$H(x,t) = -Gx + Gx_s(t) = G(x_s(t) - x) \tag{2.15}$$

Inserting Equation (2.15) into Equation (2.14), the signal can be expressed as in the form of a convolution relation [16, 20]:

$$\begin{aligned} s(t) &= B_1 m \frac{d}{dt} \int \rho(x) \mathcal{L}(kG(x_s(t) - x))\, dx \\ &= B_1 m \frac{d}{dt} \left[\rho(x) * \mathcal{L}(kGx)\right] \big|_{x=x_s(t)} \\ &= B_1 m k G \dot{x}_s(t) \left[\rho(x) * \dot{\mathcal{L}}(kGx)\right] \big|_{x=x_s(t)} \\ &= \alpha \dot{x}_s(t) \left[\rho(x) * \dot{\mathcal{L}}(kGx)\right] \big|_{x=x_s(t)} \end{aligned} \tag{2.16}$$

Here, $\alpha = B_1 mkG$ is a constant that depends on coil sensitivity, magnetic moment, and SF gradient strength. This equation expresses the MPI signal in terms of a convolution of the MNP distribution with the derivative of the Langevin function, multiplied by the instantaneous speed of the FFR.

Using this signal relation, the 1D MPI image $\hat{\rho}(x)$ can be obtained by normalizing the received signal with respect to the FFR speed $\dot{x}_s(t)$ and the constant α, and assigning the resulting speed compensated signal to the instantaneous FFR position $x_s(t)$ [16]:

$$\hat{\rho}(x_s(t)) = \frac{s(t)}{\alpha \dot{x}_s(t)} = \rho(x) * h(x)\big|_{x=x_s(t)} \tag{2.17}$$

where

$$h(x) = \dot{\mathcal{L}}(kGx) \tag{2.18}$$

Accordingly, the 1D MPI image is expressed as the convolution of the true MNP distribution $\rho(x)$ and the point spread function (PSF) $h(x)$. Here, the PSF, $h(x) = \dot{\mathcal{L}}(kGx)$, depends on both the intrinsic properties of the MNPs due to the parameter k and the selection field gradient G.

This convolution relation shows that the inherent blurring in MPI depends on both the MNP and the imaging system characteristics, and that both factors determine the spatial resolution in MPI [16]. In theory, increasing the SF gradient or the core diameter of the MNPs narrows the PSF, resulting in higher resolution MPI images. As mentioned previously, for very large MNPs, the relaxation effect becomes a limiting factor to this trend.

2.3 MPI Scanner and Overall Imaging Setup

The magnetic fields of an MPI scanner may be produced using either specialized or multi-functional electrocoil arrangements, as well as permanent magnets [21]. As an example, the imaging setup and signal flowcharts of the FFL MPI scanner at UMRAM are illustrated in Fig. 2.3. The technical details of the hardware components are explained below.

2.3.1 Selection Field Magnets

The FFR can either be a field free point (FFP) or a field free line (FFL), depending on the geometry of the SF magnets. Configurations such as opposing permanent magnets or electromagnets arranged in a Maxwell pair are commonly used to generate the SF [2, 22]. Figure 2.2 illustrates both FFP and FFL MPI scanner topologies. For the FFP MPI scanner, two disc-shaped permanent magnets are placed with their north poles facing each other, creating an FFP at the center with SF gradients of $(-4.8,\ 2.4,\ 2.4)$ T/m in $(x,\ y,\ z)$ directions [23]. In FFL MPI scanner, two sets of rectangular magnets elongated along the y-direction are placed with their north poles facing each other, creating an FFL along the y-direction with SF gradients of $(-4.4,\ 0,\ 4.4)$ T/m in $(x,\ y,\ z)$ directions. In the FFL configuration, the signal from all the MNPs along the FFL are integrated during signal reception. This results in projection-format imaging, where each measurement corresponds to the integral of the MNP distribution along the instantaneous FFL position [24].

2.3.2 Drive Coil

The drive coil that generates the DF is typically implemented as a solenoid electromagnet. For kHz range frequencies at which the DF operates, skin effect and proximity effect caused by eddy currents increase the drive coil resistance. To minimize energy losses, the drive coil is usually wound using a Litz wire.

Early MPI scanners typically utilized DF operating at approximately 25 kHz with magnetic field amplitudes ranging from 10-20 mT. Overtime, the frequency range has been expanded to 10–100 kHz, with amplitudes reaching as high as 100 mT [25]. It is essential that the DF amplitude is sufficiently strong relative to the local SF strength within the imaging volume to ensure that unsaturated MNPs near the FFR are effectively excited and detected. However, the DF amplitude is limited by biological safety considerations, such as peripheral nerve stimulation (PNS) and specific absorption rate (SAR) thresholds. Beyond the conventional sinusoidal excitation, alternative excitation schemes, such as those based on pulsed square waveforms,have also been proposed as viable options [26].

2.3.3 Transmit Chain

Due to the physical size and high number of windings, the inductance of the drive coil falls within the mH range (e.g., 0.9 mH for our FFL MPI scanner). This considerable inductance complicates efficient power transfer from the power amplifier to the drive coil, even when employing high-power amplifiers capable of delivering multiple kiloWatts. Consequently, impedance matching circuitry between the power amplifier and drive coil is employed to maximize the power transfer. This is commonly achieved using a simple matching network, such as a sizable series capacitor or a capacitor bank. However, more sophisticated multi-element matching circuits can also used [15]. Typically, impedance matching calculations are performed for a target DF frequency. Nevertheless, due to component tolerances and thermal variations (particularly in capacitors), it is challenging to achieve exact resonance at the desired frequency in practice. For example, while the intended frequency may be 10 kHz, the resonant frequency might shift slightly (e.g., 12.1 kHz for our FFL MPI scanner) due to above mentioned practical considerations and unmodeled influences such as the output impedance of the power amplifier.

When the system is resonant and the desired current is established through the drive coil, the sinusoidal DF waveform is generated either by a standalone signal generator or digitally via a data acquisition (DAQ) device interfaced with a computer. This waveform is subsequently amplified by the power amplifier connected to the impedance-matched drive coil. To ensure the correct current amplitude and thus the targeted DF amplitude within the bore, a current probe is often employed for real-time monitoring [27]. For the FFL MPI scanner in Fig. 2.3, the DF waveform is sent to the power amplifier via a DAQ card and a Rogowski current probe is employed for measuring the drive coil current.

2.3.4 Gradiometric Receive Coil

In MPI, the MNP excitation and signal receiption occurs simultaneously. As a result, the receive coil experiences a strong direct feedthrough signal caused by the inductive coupling from the time-varying DF. This direct feedthrough signal presents a significant challenge because its amplitude can be several orders of magnitude greater than that of the MNP signal, complicating the imaging process. To mitigate this issue, sinusoidal DFs are typically employed, so that the spectrum most affected by the direct feedthrough contamination corresponds to a single frequency and thus can be managed more effectively.

A common and effective method to suppress the direct feedthrough signal is the use of gradiometric receive coils [28]. These coils are wound in multiple segments with opposite winding directions, enabling cancellation of the direct feedthrough by inducing opposing voltages in the coil segments when exposed to a nearly uniform excitation field [29]. While a two-segment gradiometer coil with N-N windings (i.e., each segment having equal number of windings but wound in opposite senses) can partially reduce the direct feedthrough, it may suffer from limited sensitivity due to its spatial sensitivity profile. Hence, a three-segment configuration, with turn ratios set to approximately N-$2N$-N (where the central segment is wound opposite to the outer segments) assuming that the DF is homogeneous over the receive coil, is preferred for improved sensitivity and direct feedthrough suppression [30].

However, in practical settings, the DF is not perfectly uniform in space, causing the optimal winding ratio to deviate from the ideal values listed above. Furthermore, the DF profile may slightly vary over time due to system drift or temperature changes. Consequently, fixed-ratio gradiometric coils may not provide optimal direct feedthrough cancellation. To address this concern, receive coils with adjustable segments have been developed, allowing fine-tuning of compensation by physically shifting one of the outer segments along the coil axis [31].

2.3.5 Signal Acquisition

On the signal acquisition side, the receive coil feeds into a low-noise amplifier (LNA) that amplifies the weak signal induced by the MNPs while preserving a high signal-to-noise ratio (SNR). If residual direct feedthrough signals are not sufficiently suppressed by the gradiometric receive coil design, an analog notch filter may be introduced before amplification to attenuate the DF frequency band. However, if not accounted for, such filtering can introduce nonlinear phase shifts dependent on frequency, potentially distorting the time-domain signal and compromising downstream signal processing accuracy. Alternative methods, such as active or passive compensation circuits, can also be employed to further reduce the direct feedthrough interference and improve the fidelity of the MNP signal [32].

After amplification by LNA, the signal is digitized by a DAQ card and digitally stored on a computer for subsequent signal processing and image reconstruction steps. These signal processing typically include digital filtering of the signal to remove remaining direct feedthrough signal, and spectrum cleaning by selecting frequencies bands around the harmonics of the DF frequency to improve SNR.

2.3.6 Focus Coil and Linear Actuation

Unlike the DF, which operates in the kHz range, the FF typically functions at frequencies of only a few Hz. It produces a slow modulation that, when combined with the DF, allows the FFR to traverse a broader spatial domain. Traditionally, this field is generated via additional sets of electromagnets that are placed external to the drive coil to globally control the FFR location.

As an alternative to electromagnetic steering, the same spatial coverage can be achieved mechanically by shifting the imaging subject relative to MPI scanner. In our MPI systems, this is realized using a three-axis linear actuator that translates the imaging phantom within the scanner bore. This mechanical movement emulates the action of a dynamic FF, enabling precise relocation of the FFR across multiple imaging positions without requiring additional electromagnet coils.

2.3.7 Copper Shield

During the operation of an MPI system, time-varying magnetic fields from the drive coil can induce eddy currents on conductive structures, particularly on the surfaces of the permanent magnets responsible for generating the SF. These eddy currents may cause undesired electromagnetic interference in the receive chain. To mitigate this effect, a hollow copper cylinder is strategically positioned within the scanner bore, external to the drive coil. This copper shield acts as a preferential path for eddy current formation, effectively redirecting them away from the magnets. According to Lenz's law, the induced currents generate opposing magnetic fields that counteract the effects of the DF, thereby attenuating the alternating magnetic flux reaching the surfaces of the permanent magnets. As a result, the SF magnets are electromagnetically shielded from field fluctuations [22]. Furthermore, the high thermal conductivity of copper can also enable the shield to dissipate heat efficiently, helping to stabilize the temperature-sensitive magnetic field strength of the permanent magnets [33]. This shielding configuration contributes both to improved thermal management and to the reduction of signal artifacts, supporting consistent imaging performance.

a)

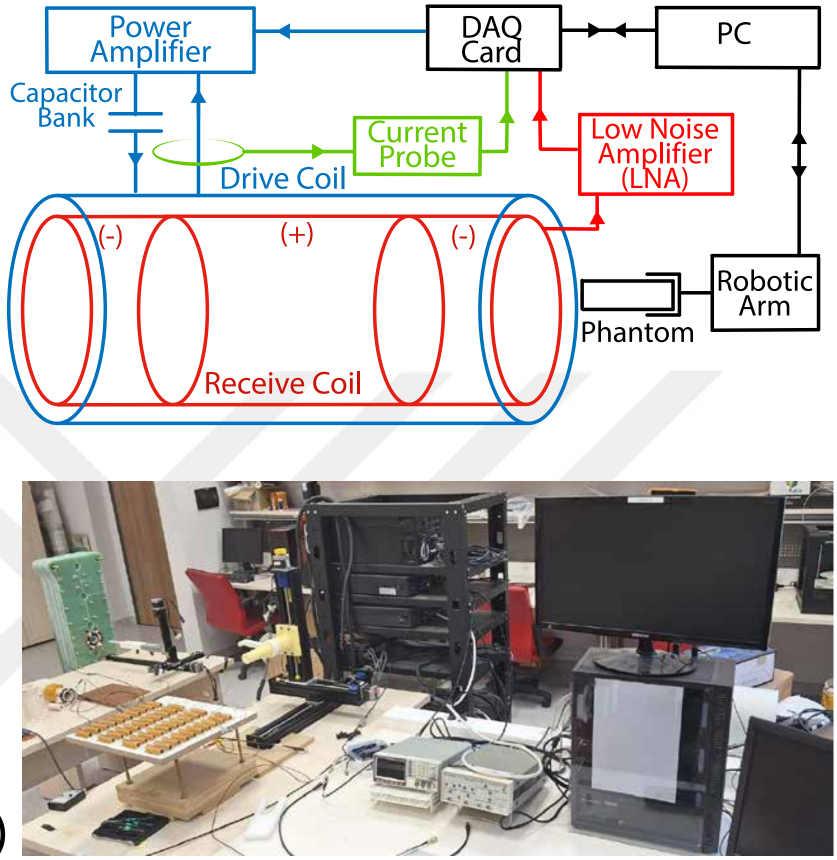

b)

Figure 2.3: The overall imaging setup of the FFL MPI scanner at UMRAM. (a) Schematic representation of the signal flowchart for the FFL scanner. The blue lines illustrate not only the drive coils responsible for generating the DF but also the complete electronic chain associated with it, including the power amplifier and the impedance matching circuitry. The red lines depict the gradiometric receive coil arrangement used for signal acquisition. Rather than employing a dedicated coil for the FF, a three-axis linear actuator is utilized to provide precise spatial positioning of the imaging phantom with respect to the FFL. The DF amplitude is continuously monitored during experiments via a Rogowski current probe integrated into the setup. (b) A photo of the FFL MPI scanner and the overall imaging setup.

Chapter 3

Saturation Field for Signal Suppression

In MPI, high concentrations of MNPs in off-target regions such as the liver can generate dominant signals that obscure weaker signals from nearby areas of interest. To address this, this thesis proposes using a saturation coil to locally apply a strong DC magnetic field, saturating the magnetization of MNPs in undesired regions. The goal of the saturation field is to suppress the contribution to the MPI signal from off-target regions, allowing improved visualization of the target tissues.

3.1 MNP Signal Suppression

In the ideal case, the magnetization of MNPs is commonly modeled using the Langevin function (see Equation (2.1)). If a sufficiently strong DC saturation field is applied in a localized region, the MNPs in that region can be driven into magnetic saturation. In this state, their magnetization will become nearly constant and unresponsive to the time-varying DF. Consequently, these saturated MNPs will cease to produce a signal, effectively removing their contribution from the MPI image. This principle can enable precise spatial control over the active imaging volume by selectively suppressing signals from undesired regions.

3.1.1 Signal Equation with Saturation Field

To determine how the saturation field affects the MPI signal, first the spatial distribution of MNPs are modeled as being decomposed of two parts: (1) MNPs located in the region of interest (target) and (2) MNPs accumulated in the undesired anatomical regions (off-target). For the 1D case, this decomposition can be expressed as follows:

$$\rho(x) = \rho_{\text{target}}(x) + \rho_{\text{off}}(x) \tag{3.1}$$

where $\rho_{\text{target}}(x)$ and $\rho_{\text{off}}(x)$ represent the distribution of MNPs within the target and off-target regions, respectively (see Figure 3.1).

As explained previously, during MPI acquisition, the MNPs are exposed to a superposition of magnetic fields, mainly the DF and the SF (see Equation (2.9)). This thesis proposes applying an additional DC saturation field that varies as a function of space but is static in time. The resulting total magnetic field at position x and time t can then be written as:

$$\begin{aligned} H(x,t) &= H_s(x) + H_d(t) + H_{sat}(x) \\ &= -Gx + H_{\text{peak}}\cos(2\pi f_d t) + H_{\text{sat}}(x) \end{aligned} \tag{3.2}$$

Here, $H_{\text{sat}}(x)$ is a spatially localized DC field introduced to saturate MNPs in the off-target regions. Assuming that $H_{\text{sat}}(x)$ does not change the position of the FFR, it follows that:

$$H(x,t) = G(x_s(t) - x) + H_{\text{sat}}(x) \tag{3.3}$$

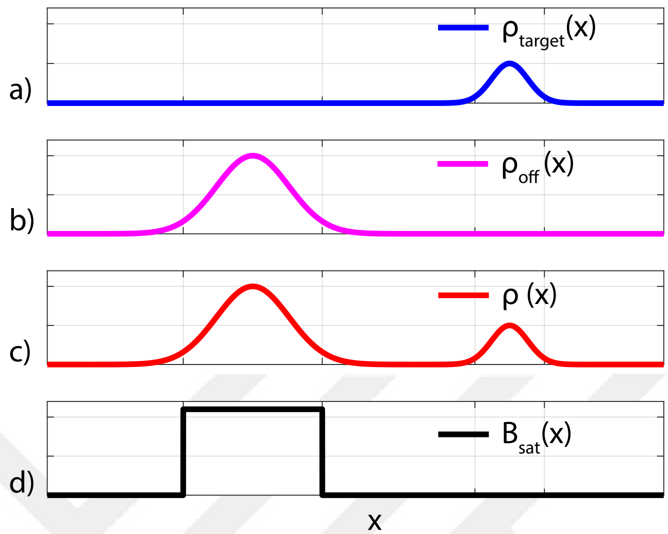

Figure 3.1: Spatial distributions of MNPs and the saturation field profile. (a) The target region distribution, $\rho_{\text{target}}(x)$, representing MNPs within the region of interest only. (b) The off-target distribution, $\rho_{\text{off}}(x)$, representing MNPs accumulated outside the target region. (c) The combined MNP distribution, $\rho(x) = \rho_{\text{target}}(x) + \rho_{\text{off}}(x)$. (d) The spatial profile, $B_{sat}(x)$, for an ideal (albeit infeasible) saturation field. The saturation field selectively covers the off-target region, aiming to suppress the unwanted signal contribution from $\rho_{\text{off}}(x)$ without affecting the target region.

As illustrated in Figure 3.1, in the ideal (albeit infeasible) case, $H_{\text{sat}}(x)$ can be modeled as a rectangle function in space, i.e., equal to H_{sat} on the target region and zero elsewhere. For this ideal case, inserting Equation (3.1) and Equation (3.3) into Equation (2.16), the MPI signal can be expressed as:

$$s(t) = \alpha \dot{x}_s(t) \left[\rho_{\text{target}}(x) * \dot{\mathcal{L}}(kGx) + \rho_{\text{off}}(x) * \dot{\mathcal{L}}(k(Gx + H_{\text{sat}})) \right] \Big|_{x=x_s(t)} \tag{3.4}$$

3.1.2 Image Equation with Saturation Field

Compensating the previous signal equation by FFR speed, the corresponding 1D MPI image can be written as:

$$
\begin{aligned}
\hat{\rho}(x_s(t)) &= \frac{s(t)}{\alpha \dot{x}_s(t)} \\
&= \left[\rho_{\text{target}}(x) * \dot{\mathcal{L}}(kGx) + \rho_{\text{off}}(x) * \dot{\mathcal{L}}(k(Gx + H_{\text{sat}}))\right] \big|_{x=x_s(t)} \\
&= \left[\rho_{\text{target}}(x) * h(x) + \rho_{\text{off}}(x) * h\left(x + \frac{H_{\text{sat}}}{G}\right)\right] \big|_{x=x_s(t)} \\
&= \left[\rho_{\text{target}}(x) * h(x) + \rho_{\text{off}}(x) * h(x + \Delta x_{\text{sat}})\right] \big|_{x=x_s(t)}
\end{aligned}
\tag{3.5}
$$

where

$$\Delta x_{\text{sat}} = \frac{H_{\text{sat}}}{G} \tag{3.6}$$

Here, $h(x) = \dot{\mathcal{L}}(kGx)$ is the PSF of the imaging system (see Equation (2.18)). As seen in this equation, the goal of saturation field is to suppress the image contribution from the off-target region by shifting the effective PSF experienced by the off-target MNPs to outside the sensitive region of the Langevin function's derivative. Using translation equivariance of convolution operation, this equation can be re-written as follows:

$$
\begin{aligned}
\hat{\rho}(x_s(t)) &= \left[\rho_{\text{target}}(x) * h(x) + \rho_{\text{off}}(x + \Delta x_{\text{sat}}) * h(x)\right] \big|_{x=x_s(t)} \\
&= \hat{\rho}_{\text{target}}(x_s(t)) + \hat{\rho}_{\text{off}}(x_s(t) + \Delta x_{\text{sat}})
\end{aligned}
\tag{3.7}
$$

where

$$
\begin{aligned}
\hat{\rho}_{\text{target}}(x) &= \rho_{\text{target}}(x) * h(x) \\
\hat{\rho}_{\text{off}}(x) &= \rho_{\text{off}}(x) * h(x)
\end{aligned}
\tag{3.8}
$$

Here, $\hat{\rho}_{\text{target}}(x)$ and $\hat{\rho}_{\text{off}}(x)$ are image contributions in the absence of saturation field for the target and off-target regions, respectively. This alternative formulation shows that the saturation field spatially shifts $\hat{\rho}_{\text{off}}(x)$ by Δx_{sat}. Then, the goal of saturation field is to apply a sufficiently large spatial shift, Δx_{sat}, so that the image contribution from the off-target region does not overlap with that of the target region, i.e.,

$$\hat{\rho}(x) \approx \hat{\rho}_{\text{target}}(x), \;\; x \in \text{FOV} \tag{3.9}$$

As seen in Equation (3.6), Δx_{sat} depends on both the applied saturation field H_{sat} and the SF gradient G, with larger H_{sat} needed for larger G. In addition, since the width of the PSF is a function of the MNP parameter k, the shift also depends on the MNP parameters, such as the core diameter.

Hence, by carefully selecting the DC field strength and spatial profile of $H_{\text{sat}}(x)$, one can in theory suppress the signal originating from off-target regions, thereby improving image quality.

3.2 Simulation-Based Determination of Saturation Field Strength

3.2.1 Imaging Simulations:

To determine the DC saturation field strength required to effectively suppress signals from off-target MNPs, a set of numerical simulations was conducted using MATLAB. These simulations were designed to model the magnetization response of MNPs under the combined influence of the oscillatory DF, the SF, and an externally applied DC saturation field. The DF was set at 25 kHz with 10 mT amplitude, and the SF gradients were set as (2.4, 2.4, -4.8) T/m in (x, y, z) directions based on our in-house FFP MPI scanner. MNPs at two different core diameters of $d_c = 20$ nm and $d_c = 25$ nm were considered. Assuming magnetite MNPs, the saturation magnetization was set as $M_{\text{sat}} = 0.6$ T$/\mu_0$, where μ_0 is the vacuum permeability [16]. The MNP signal was computed using Equation (2.14), assuming ideal Langevin response for MNPs. FOV was set as 2×2 cm^2.

As shown in Fig.3.2, two different imaging phantoms were created: (1) a reference phantom containing only a vessel-shaped target region (i.e., ρ_{target} only), and (2) a phantom containing both the vessel-shaped target and a high-concentration off-target region (i.e., containing both ρ_{target} and ρ_{off}). The MPI image from the reference phantom was used as a reference image for quantitative and qualitative evaluations.

The saturation field, B_{sat}, was varied from 0-100 mT. For each B_{sat} value, reconstructed MPI images were compared to the reference image. Quantitative image quality assessment were performed using the peak signal-to-noise ratio (PSNR) metric defined as follows:

$$PSNR = 10\ \log_{10}\left(\frac{MAX_I^2}{MSE}\right) \tag{3.10}$$

where

$$MSE = \frac{1}{mn}\sum_{i=0}^{m-1}\sum_{j=0}^{n-1}\left[I(i,j) - I_{\text{ref}}(i,j)\right]^2 \tag{3.11}$$

where I is the reconstructed image, I_{ref} is the reference image, and m and n are their dimensions. MAX_I is the maximum pixel intensity of I_{ref}, and MSE measures the mean squared error difference between I and I_{ref}.

3.2.2 Qualitative Results:

As shown in Fig.3.2(c), first, a saturation field with an ideal rectangular profile was selectively applied to the off-target region. The FOV was placed such that it did not overlap with the off-target region. Figure 3.3 shows example reconstructed images and the corresponding absolute error maps for B_{sat} ranging from 0-50 mT, separately for the cases of $d_c = 20$ nm and $d_c = 25$ nm. These results demonstrate that for $B_{\text{sat}} = 0$ mT, the high-intensity signal from the off-target region spreads onto the target region, deteriorating the image quality. As B_{sat} increases, off-target signal suppression improves, leading to higher image quality.

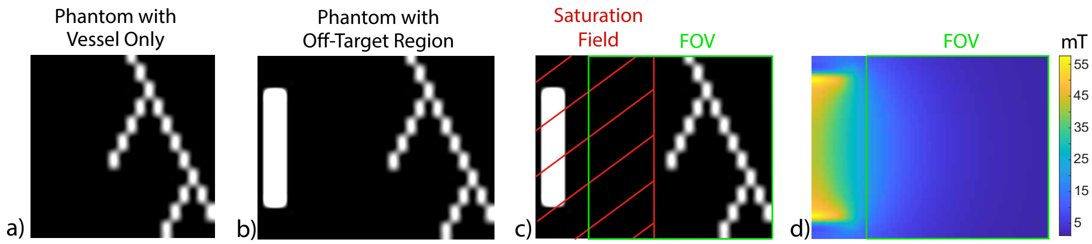

Figure 3.2: Imaging phantoms and saturation field setups used in the simulation study. (a) Reference phantom containing only a vessel-shaped target region. (b) Phantom including both the vessel-shaped target and a high-concentration off-target region (concentration ratio of 1:5). (c) Visualization of the ideal saturation field (red shaded area) selectively targeting the off-target region, with the field-of-view (FOV) (green rectangle). (d) Simulated saturation field profile of a realistic saturation coil, showing high field strength localized over the off-target region and minimal exposure within the target region.

Next, considering that a rectangular magnetic field profile is infeasible, the magnetic field profile for a realistic saturation coil with 16 turns wound on a 1.5 cm diameter was simulated. As shown in Fig. 3.2(d), the resulting saturation field is strong over the off-target region. Importantly, unlike the ideal case, the saturation field extends into the imaging FOV and the target region. Figure 3.4 shows example reconstructed images and the corresponding absolute error maps for B_{sat} ranging from 0-50 mT, separately for the cases of $d_c = 20$ nm and $d_c = 25$ nm. Here, B_{sat} is defined as the B-field at the coil center. Once again, the image quality first improves with increasing B_{sat}. However, large B_{sat} values also perturb the target image region due to partial signal suppression and slight spatial shifting.

3.2.3 Quantitative Results:

A quantitative summary of the imaging simulations is presented in Fig. 3.5, where PSNR is plotted as a function of B_{sat} for the ideal and realistic coil cases, for $d_c = 20$ nm and $d_c = 25$ nm. In the ideal case (dashed lines), PSNR increases consistently with B_{sat}. In the realistic case (solid lines), PSNR keeps increasing for B_{sat} ranging upto 40-50 mT, but eventually starts decreasing due to increased

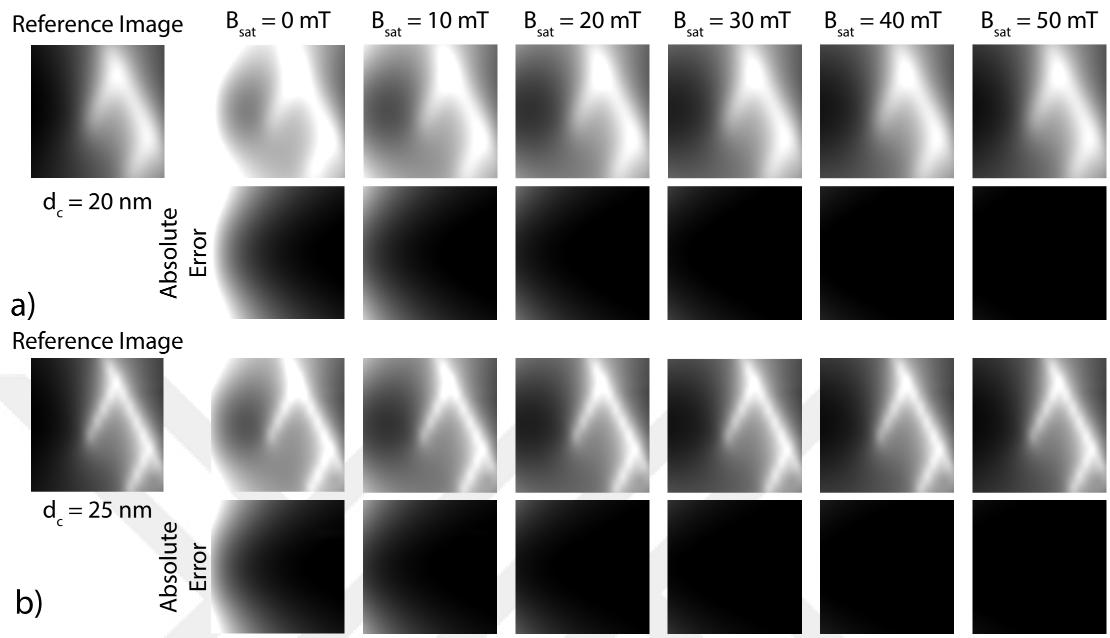

Figure 3.3: Simulated MPI images for the ideal saturation field in Fig.3.2(c), demonstrating the impact of B_{sat} on signal suppression for two different MNP core diameters: (a) $d_c = 20$ nm and (b) $d_c = 25$ nm. In each case, the leftmost column shows the reference image (phantom with vessel only), while the subsequent columns show reconstructed images under different B_{sat} values applied to the off-target region. The second row in each subfigure displays the corresponding absolute error maps relative to the reference image. In this ideal case, a uniform DC saturation field is applied over the off-target region, with zero field over the target region.

saturation field spillover into the target region at higher field strengths.

Overall, the results show that increasing B_{sat} improves suppression performance up to a certain field strength, beyond which further increases yield minimal gains and potential damages. For both core sizes, a saturation field strength of approximately 40-50 mT was found to be sufficient for effective off-target suppression and was used as the design target for the saturation coil in the subsequent experimental studies.

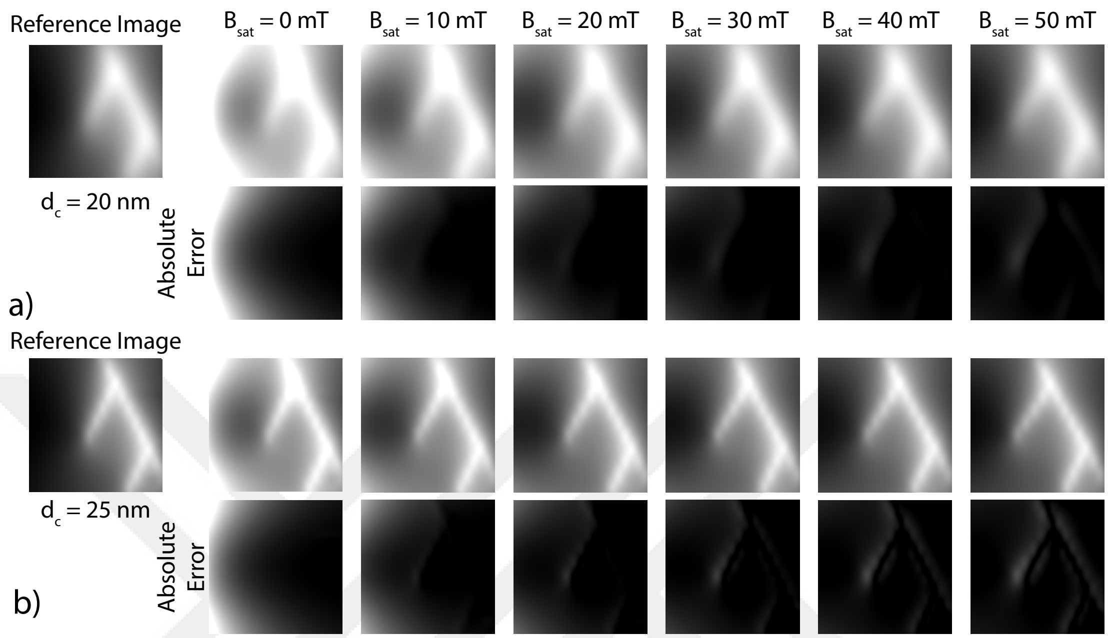

Figure 3.4: Simulated MPI images for the realistic saturation field case in Fig.3.2(d), demonstrating the impact of B_{sat} on signal suppression for two different MNP core diameters: (a) $d_c = 20$ nm and (b) $d_c = 25$ nm. In this realistic case, the saturation field is simulated via realistic coil parameters, resulting in a non-uniform DC saturation field over the off-target region, which partially affects the target region, especially at high B_{sat} values.

3.3 Integrating Saturation Coil into MPI Scanner

The integration of a saturation coil into the MPI scanner introduces new interactions between the hardware components that must be carefully analyzed. These interactions directly influence the received signal and overall image quality. To understand the effects of the saturation coil on signal acquisition, this thesis first formulates the components of the induced voltage on the receive coil.

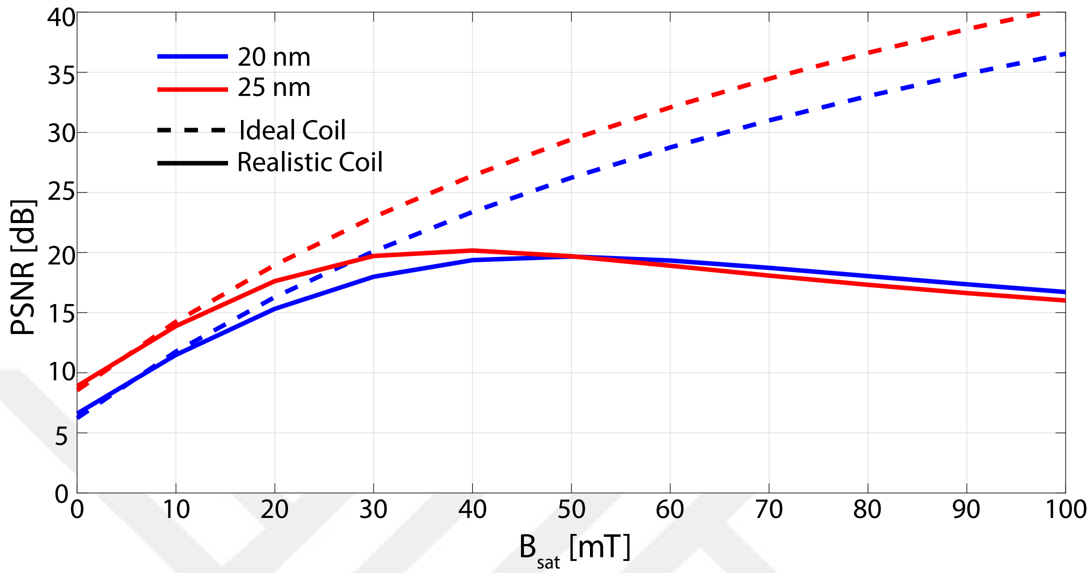

Figure 3.5: Image quality as a function of B_{sat} for the ideal (dashed) and realistic (solid) coil cases, for two different MNP core sizes of 20 nm (blue) and 25 nm (red). While PSNR increases steadily in the ideal case, it peaks at around 40-50 mT and declines thereafter in the realistic case, due to field spillover into the target region at higher B_{sat} values.

3.3.1 Formulation of Baseline Signal

When the saturation coil is integrated into the MPI system, the DF induces eddy currents and voltages on the saturation coil, which in turn induce an undesired baseline signal on the receive coil. The following derivation assume that the saturation coil is placed around a specific part of the phantom to locally suppress the signal from that region. During imaging, the saturation coil is moved inside the receive chamber of the MPI scanner together with the phantom, at a constant speed v in the z-direction. Without loss of generality, the following derivations also assume that the DF is homogeneous in space and can be expressed as $B_d(t) = B_p sin(\omega t)$. The total baseline signal induced on the receive coil (i.e., the voltage in the absence of MNPs) can then be expressed as a superposition of three separate components:

$$\varepsilon_B(t) = \varepsilon_1(t) + \varepsilon_2(t) + \varepsilon_3(t) \tag{3.12}$$

Here, $\varepsilon_1(t)$ is the direct feedthrough voltage induced on the receive coil due to the DF, whereas $\varepsilon_2(t)$ and $\varepsilon_3(t)$ are the induced voltages over the receive coil due to the secondary fields created by the saturation coil and the eddy currents on the saturation coil, respectively. These induced voltages can be approximated as follows (see Appendix for detailed derivations):

$$\begin{aligned}
\varepsilon_1(t) =& -A_r B_p \omega cos(\omega t) \sum_{i=1}^{N_r} W_{r,i} \\
\varepsilon_2(t) \approx& -A_s N_s B_p \frac{\omega^2}{|Z_s|} sin(\omega t - \theta_s) \\
&\times \sum_{i=1}^{N_r} W_{r,i} \iint_{A_r} S_s(x, y, z_{r,i} - vt) dxdy \\
\varepsilon_3(t) \approx& -\pi B_p \omega^2 \left(\frac{R_o^2}{|Z_o|} sin(\omega t - \theta_o) - \frac{R_{in}^2}{|Z_{in}|} sin(\omega t - \theta_{in}) \right) \\
&\times \sum_{i=1}^{N_r} W_{r,i} \iint_{A_r} S_s(x, y, z_{r,i} - vt) dxdy
\end{aligned} \tag{3.13}$$

Here, A_r is the axial cross-sectional area of the receive coil, N_r is the number of receive coil windings, and $W_{r,i} = \pm 1$ is the winding sense of the i^{th} winding of the gradiometric receive coil located at position $z_{r,i}$ with respect to the scanner isocenter. In addition, A_s is the axial cross-sectional area of the saturation coil, N_s is the number of saturation coil windings, $Z_s = |Z_s|e^{j\theta_s}$ is the impedance seen by the saturation coil at the DF frequency, and $S_s(x, y, z)$ is the position-dependent saturation coil efficiency (i.e., magnetic flux along the z-direction per unit current through the saturation coil). Furthermore, R_o and R_{in} are the outer and inner radii of the saturation coil (with the difference filled with solid copper windings), and $Z_o = |Z_o|e^{j\theta_o}$ and $Z_{in} = |Z_{in}|e^{j\theta_{in}}$ are the impedances seen by the eddy currents flowing on the outer and inner surfaces of the saturation coil, respectively. The formation of eddy currents are illustrated in Fig. 3.6.

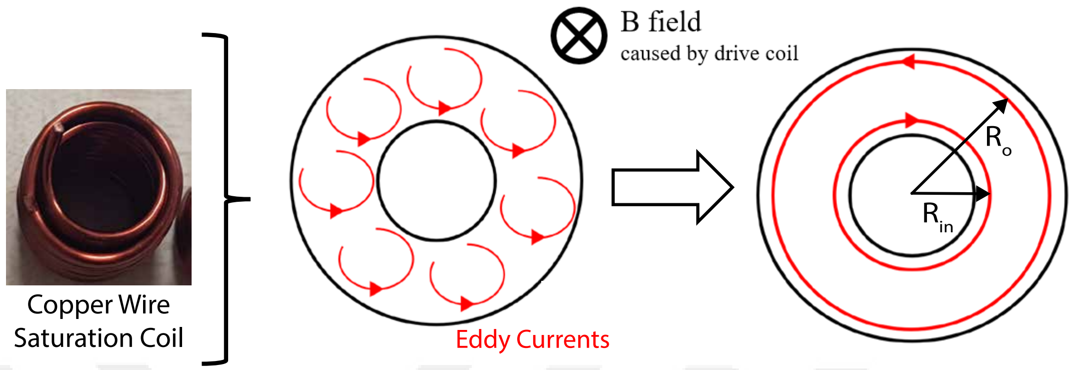

Figure 3.6: Schematic illustration of eddy current formation in a saturation coil wound using a solid copper wire. When the saturation coil is exposed to a time-varying magnetic field generated by the drive coil, eddy currents form within the copper wires, as marked with the red arrows (middle), which effective add up to two circular currents in opposing directions flowing on the outer and inner surface of the wire (right).

As seen in these equations, all induced baseline signals over the receive coil are directly proportional to the DF amplitude, B_p. Here, the direct feedthrough signal, $\varepsilon_1(t)$, has a constant amplitude. In contrast, the amplitudes of $\varepsilon_2(t)$ and $\varepsilon_3(t)$ depend on time due to the movement of the saturation coil inside the MPI scanner.

The impedances in the equations for $\varepsilon_2(t)$ and $\varepsilon_3(t)$ depend on the DF frequency, ω. For example, the proportionality between the frequency and the induced voltages can be expressed with ω, and $\frac{\omega^2}{|Z_s|}$, for $\varepsilon_1(t)$, and $\varepsilon_2(t)$, respectively. Additionally, the phase differences, θ_s, θ_o, and θ_{in}, also depend on the DF frequency.

3.3.2 Strategies for Reducing Baseline Signal

As stated above, in the experiments conducted in this thesis, the saturation coil moves together with the phantom inside the scanner at a constant velocity, v. As a result, the saturation coil is exposed to the DF and generates secondary fields over the receive coil. During the imaging experiments, the voltage on the receive coil consists of the baseline signal and the MNP signal. Typically, the baseline signal is significantly larger than the MNP signal. Fortunately, the baseline signal appears at the fundamental frequency, while the MNP signal appears at the harmonics. Therefore, during the post-processing step, the fundamental frequency is filtered out, and the remaining MNP signal is utilized for image reconstruction. However, the high baseline signal on the receive coil limits the low-noise-amplifier (LNA) gain, causing the higher harmonics of the MNP signal to be buried under noise. As a result, the reconstructed image quality suffers at low LNA gains. The primary objective, therefore, is to reduce the baseline signal on the receive coil as much as possible.

As shown in Equation (3.13), the baseline signal on the receive coil (ε_B) consist of ε_1, ε_2, and ε_3, which are due to the direct feedthrough, the secondary fields from the saturation coil, and the eddy currents on the saturation coil, respectively. As explained previously, the direct feedthrough is a common problem in MPI and is not the topic of this thesis. To decrease ε_1, the receive coil is wound in a gradiometric configuration, aiming to eliminate the induced voltage from the DF by reducing the term $\sum_{i=1}^{N_r} W_{r,i}$ to nearly zero.

To decrease ε_2, the impedance seen by the saturation coil, Z_s, can be increased. However, there is a constraint in this context. During the experiments, a DC current source is utilized for supplying a DC current through the saturation coil, which has a very low DC resistance. Adding a resistance in series with the saturation coil would also increase the impedance seen by the DC current source. However, due to the power limitations of the DC current source, increasing the DC resistance beyond a few Ohms restricts the saturation field strength. Hence, the goal is to increase the impedance seen by the saturation coil at DF frequency without significantly affecting the DC resistance seen by the DC current source. To achieve this goal, this thesis proposes placing a large, air-core L-choke inductor in series with the saturation coil: the L-choke introduces a high impedance at DF frequencies, while maintaining a low DC resistance, as described in detail in the following chapter.

To decrease ε_3, the formation of eddy currents need to be minimized. To address this goal, this thesis proposes using Litz wire instead of solid copper wire for winding the saturation coil. When a Litz wire is used, eddy currents are minimized as a result of the electrically insulated strands it contains. Insulated strands in the Litz wire limits the formation of large loops of eddy currents, such that ε_3 becomes negligibly small.

Chapter 4

Materials and Methods

Parts of this chapter are based on the following publications:

> E Kor, MT Arslan, EU Saritas. "Saturation Coil for Localized Signal Suppression in MPI", *Proc of the 11th International Workshop on Magnetic Particle Imaging (IWMPI)*, Virtual Conference, p. 2203013, March 2022.
>
> E Kor, MT Arslan, M Takrimi, EU Saritas. "Preventing Interference Between Saturation Coil and Receive Coil in MPI", *Proc of the 13th International Workshop on Magnetic Particle Imaging (IWMPI)*, Flueli-Ranft, Switzerland, p. 2403003, March 2024.

4.1 Interference Experiments

To investigate the potential sources and characteristics of the baseline signal interference for an MPI scanner with added saturation coil, a series of experiments were performed. Since the direct feedthrough signal is already mitigated by utilizing a gradiometric receive coil, the experiments were designed to focus on the remaining two contributors of the baseline signal: eddy currents on the saturation

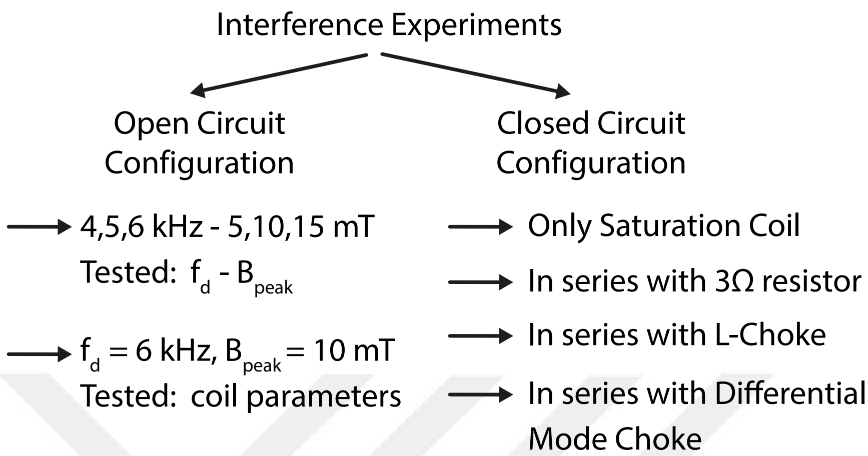

Figure 4.1: Summary of interference experiments.

coil and secondary fields created by the saturation coil. These interferences can significantly degrade image quality by inducing unwanted signals.

Figure 4.1 summarizes the interference experiments. The experiments were conducted on our in-house FFL MPI scanner as seen in Fig 4.2(a-c). This scanner features selection field gradients of (-4.4, 0, 4.4) T/m in the (x, y, z) directions, and has a free imaging bore diameter of 3.5 cm.

4.1.1 Interference Due to Eddy Currents

First, experiments were performed with the saturation coil in open-circuit configuration. This configuration makes Z_s in Equation (3.13) infinitely large, therefore removes the baseline signal contribution from $\varepsilon_2(t)$.

To verify the dependence of $\varepsilon_3(t)$ on B_p and w as given in Equation (3.13), an arbitrary waveform (AW) MPI scanner was utilized [34]. As shown in Fig 4.2(a), our FFL MPI scanner was equipped with a very low inductance drive coil that does not require any impedance matching to the power amplifier, enabling arbitrary selection of DF frequency. Using this AW MPI scanner, the DF was applied at different frequencies and amplitudes along the z-direction. Combinations of f_d = 4, 5, and 6 kHz frequencies with B_p = 5, 10, and 15 mT amplitudes were tested. A saturation coil wound using a solid copper wire with 1.2 mm diameter was utilized. The saturation coil consisted of 2 layers, each with 16 windings, and had an inner diameter of 1.1 cm. In these experiments, the saturation coil was moved along a line by a linear actuator at a speed of 3 cm/s, in the abscence of MNPs. The baseline signal was acquired over a 1D FOV of 16.8 cm along the z-direction, within a total scan time of approximately 5.6 s.

Next, the DF was applied at 6 kHz with 10 mT, and different saturation coil designs were tested in an open-circuit configuration . The impact of the number of layers and windings of the saturation coil on the receive coil was evaluated. The inner diameter of the coils and the wire diameter were kept the same as before. In the final stage of the experiments, different wire types were compared. The performances of saturation coils wound using solid copper wire and Litz wire were evaluated, all in the open-circuit configuration.

4.1.2 Interference Due to Secondary Fields

In the second part of the interference experiments, the saturation coil was utilized in a closed-circuit configuration, i.e., connected in series with a DC current source. For these experiments, a saturation coil wound using a Litz wire (1.2 mm diameter, 125 strands) was utilized. This saturation coil had 2 layers with 16 windings each, with an inner diameter of 1.5 cm. As shown later, utilizing a Litz wire eliminates the eddy currents on the saturation coil, so that the baseline signal contribution from $\varepsilon_3(t)$ can be ignored.

These experiments were performed using our FFL MPI scanner equipped with its standard drive coil as shown in as shown in Fig. 4.2(b). The standard drive coil had medium-scale inductance, and hence required impedance matching to the power amplifier at the DF frequency. Experiments were performed at f_d = 12.1 kHz and B_p = 10 mT along the z-direction. In these experiments, the saturation coil was moved by a linear actuator at a speed of 3 cm/s. The baseline signals were acquired in a 1D FOV of 9.1 cm along the z-direction, within a total scan time of approximately 3 s.

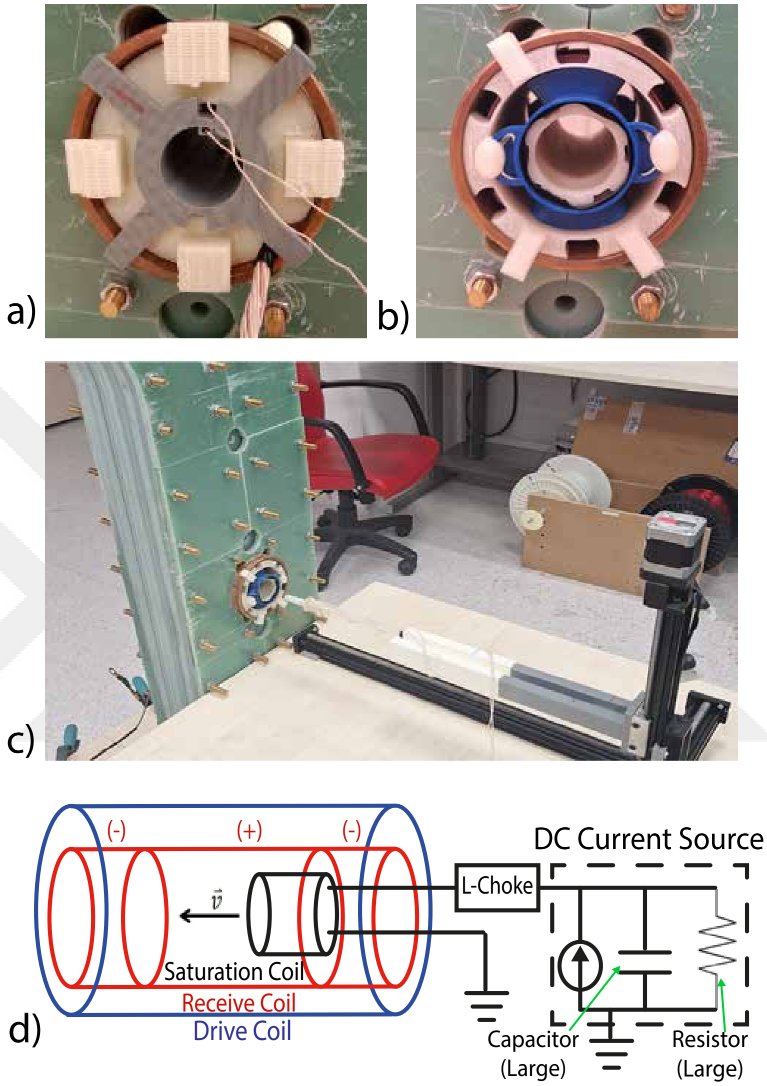

Figure 4.2: Experimental setups used in the interference experiments. (a) Open-circuit configuration interference experiments were performed at DF frequencies of 4, 5, and 6 kHz to study the interference due to the eddy current effects (i.e., ε_3). A low inductance drive coil that does not require any impedance matching was utilized, converting our FFL MPI scanner to an arbitrary waveform (AW) MPI scanner. (b) Closed-circuit configuration interference experiments were performed with a standard drive coil that is impedance matched to the power amplifier at 12.1 kHz, to study the interference due to secondary fields (i.e., ε_2). (c) The overall MPI scanner setup, including the phantom and linear actuator system, and (d) the schematic of the overall setup used in the imaging experiments, showing the saturation coil moving inside the imaging region, with an L-choke connected in series.

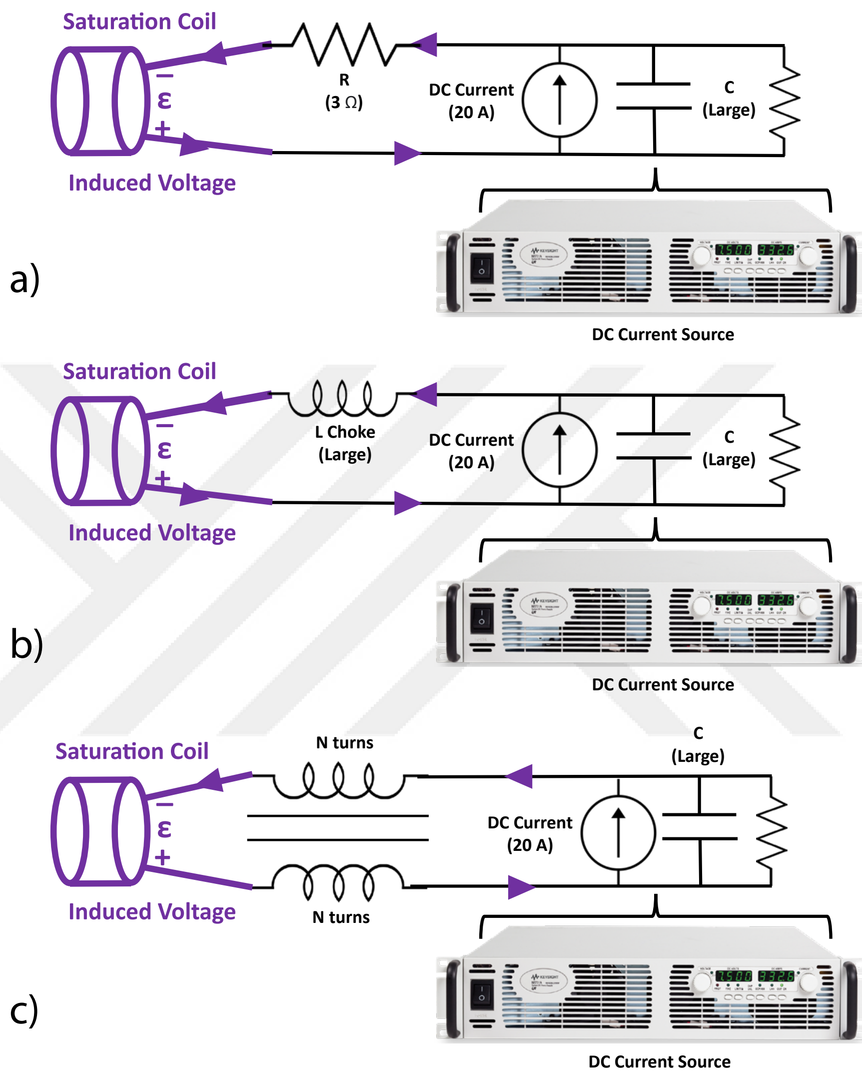

Figure 4.3: Schematic representations of potential solutions for suppressing interference due to secondary fields. (a) a resistor (3 Ω) connected in series with the saturation coil, (b) an air-core L-choke, and (c) differential-mode choke.

Different techniques to increase Z_s, the impedance seen by the induced voltage across the saturation coil at the DF frequency, were tested and compared. The received signals were analyzed for the following cases:

1. No additional impedances,
2. A 3 Ω resistor connected in series with the saturation coil (see Fig. 4.3(a)),

3. A large air-core L-choke connected in series with the saturation coil (see Fig. 4.3(b)),

4. A differential mode choke connected between the saturation coil and the DC current source (see Fig. 4.3(c)). Here, the effect of DC current on the performance of the differential mode choke was evaluated for 0 A and 20 A DC currents.

4.2 Imaging Experiments

The imaging experiments were conducted on our in-house FFL MPI scanner equipped with the standard drive coil (see Fig. 4.2(b)). The DF was applied at $f_d = 12.1$ kHz and $B_p = 10$ mT along the z-direction. Images were acquired over a 1D FOV of 9.1 cm along the z-direction. The linear actuator moved at a speed of 3 cm/s, with a total scan time of approximately 3 s.

The received signals were first amplified using an LNA and subsequently digitized via a data acquisition card (DAQ). To extract the MNP signal, the baseline signal for the direct feedthrough (i.e., acquired without the phantom or the saturation coil) was subtracted from the measured signal. Next, a direct feedthrough filter (i.e., a high-pass filter) was applied to suppress the fundamental harmonic component. Image reconstruction was performed using the x-space-based Partial Field-of-View Center Imaging (PCI) algorithm [32]. Table 4.1 lists the devices and their models used in the imaging experiments. Fig. 4.4 summarizes the imaging experiments.

4.2.1 Saturation Coil & Phantom Design

During the experiments, different types of saturation coils were tested. All coils had 1.5 cm inner diameter and were wound using a Litz wire with 1.2 mm diameter and 125 strands. First, a solenoidal saturation coil with 2 layers and 16 windings

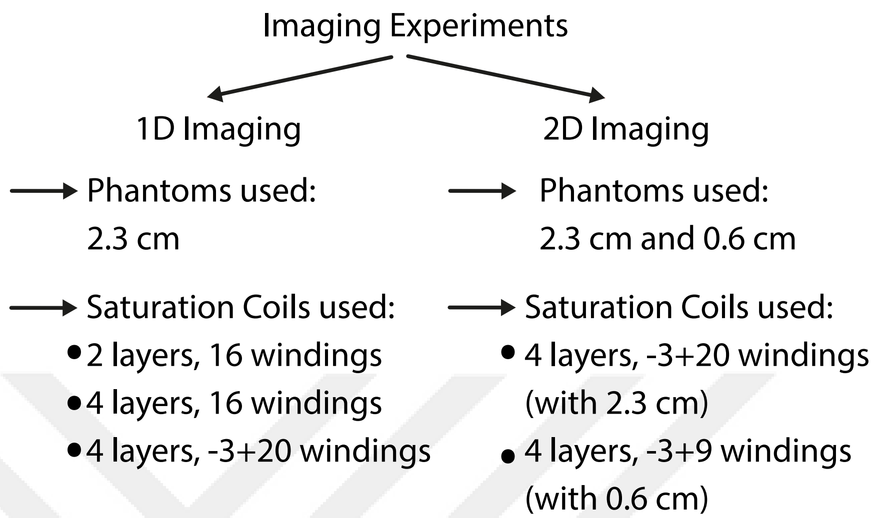

Figure 4.4: Summary of imaging experiments.

Table 4.1: List of main laboratory instruments used in the MPI experimental setup, including device types and their corresponding models.

Device	**Brand / Model**
Low Noise Amplifier (LNA)	SRS SR560
DAQ Card	NI USB-6383
Current Probe	PEM LFR 06/6/300 (Rogowski)
Linear Actuator	Velmex BiSlide
Power Amplifier	AE Techron 7224
DC Source	Keysight N8700 Series

per layer, and another with 4 layers and 16 windings per layer were compared. These two solenoidal coils have windings in the same sense, as seen in Fig 4.5(a,b). As a result, the B-field profiles of these saturation coils are relatively wide, causing the target sample to be slightly affected by the saturation field.

As an alternative design, two reverse-wound saturation coils with 4 layers were developed to ensure that the target sample is not affected by the saturation field. To achieve this, an improved 4-layer saturation coil with 3 reverse windings and 20 forward windings per layer was implemented as seen in Fig 4.5(c). In addition, another 4-layer improved saturation coil with 3 reverse windings and 9 forward windings per layer was implemented as seen in Fig 4.5(d).

In total, four different saturation coils were designed and tested, as shown in

Fig. 4.5(a-d). The B-field profiles of these coils for the case of 20 A DC current are compared in Fig. 4.6, showing that the improved coils with reverse windings have sharper B-field profiles.

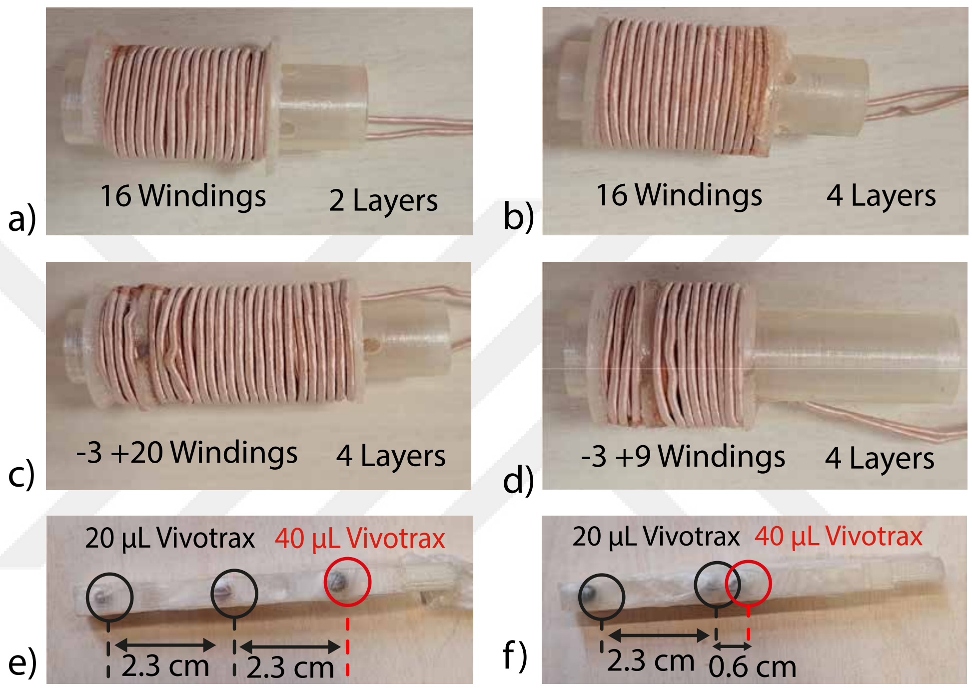

Figure 4.5: The saturation coils and phantoms used in the imaging experiments. (a)–(d) The four saturation coils: (a) solenoidal 2-layer coil, with 16 windings per layer coil; (b) solenoidal 4-layer coil, with 16 windings per layer; (c) improved 4-layer coil, with 3 reverse windings and 20 forward windings per layer (labeled as -3+20 windings); (d) improved 4-layer coil, with 3 reverse windings and 9 forward windings per layer (labeled as -3+9 windings). (e-f) The two imaging phantoms: (e) the phantom with the off-target region (red) located farther from the target region, with 2.3 cm separation; (f) the phantom with the off-target region (red) located closer to the target region, with 0.6 cm separation.

Two custom-designed phantoms were prepared to evaluate the performances of the different saturation coil designs. Each phantom consisted of a target region containing two spatially separated 20 μL undiluted Vivotrax (5.5 mg Fe/mL undiluted concentration) samples and an off-target region containing a single 40 μL undiluted Vivotrax sample, as seen in Fig. 4.5(e,f). To analyze the signal suppression performance, the off-target region was positioned at two different distances of 2.3 cm and 0.6 cm from the target.

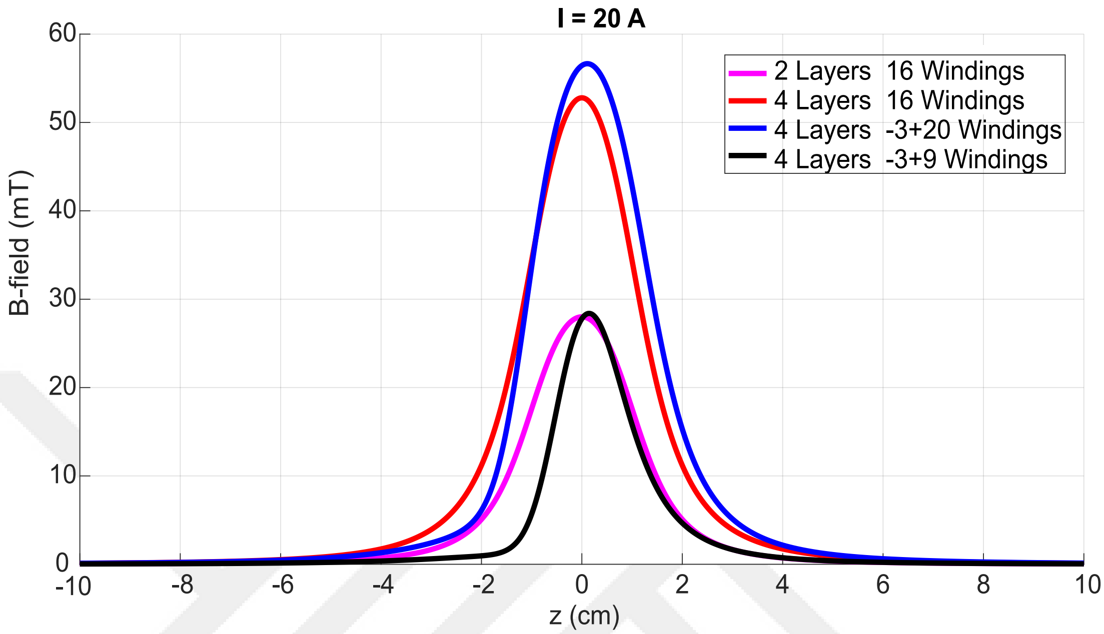

Figure 4.6: Simulated magnetic field profiles of the saturation coils used in the imaging experiments for $I = 20$ A. The comparison includes: 2-layer, 16 windings coil (magenta); 4-layer, 16 windings coil (red); 4-layer improved coil with -3+20 windings (blue); and 4-layer improved coil with -3+9 windings (black).

4.2.2 1D Imaging Experiments

First, the phantom with an off-target separation of 2.3 cm was used as seen in Fig 4.5(e). To evaluate the effectiveness of the improved saturation coil, 1D images obtained using saturation coils with 2 layers and 16 windings, 4 layers and 16 windings, and an improved saturation coil with 4 layers and -3+20 windings were compared. The 2-layer saturation coil generated a magnetic field of 28 mT over the off-target sample, whereas the 4-layer coil with 16 windings produced 52 mT. The improved saturation coil yielded approximately 54 mT.

4.2.3 2D Imaging Experiments

Second, a more challenging scenario was evaluated using a phantom with an off-target separation of just 0.6 cm, as shown in Fig. 4.5(f). In this experiment, the performance of an improved 4-layer saturation coil with -3+9 windings was assessed and compared to that of an improved 4-layer coil with -3+20 windings, which had previously been tested using a phantom where the off-target separation was 2.3 cm. Despite its lower number of windings, the improved coil with -3+9 windings generated a magnetic field of 28 mT over the off-target region. In comparison, the improved coil with -3+20 windings produced 54 mT over the off-target region. These experiments aimed to demonstrate the effectiveness of the improved coil design in maintaining spatial selectivity across varying off-target distances.

Chapter 5

Experimental Results

Parts of this chapter are based on the following publications:

> E Kor, MT Arslan, EU Saritas. "Saturation Coil for Localized Signal Suppression in MPI", *Proc of the 11th International Workshop on Magnetic Particle Imaging (IWMPI)*, Virtual Conference, p. 2203013, March 2022.
>
> E Kor, MT Arslan, M Takrimi, EU Saritas. "Preventing Interference Between Saturation Coil and Receive Coil in MPI", *Proc of the 13th International Workshop on Magnetic Particle Imaging (IWMPI)*, Flueli-Ranft, Switzerland, p. 2403003, March 2024.

5.1 Interference Experiment Results

Two distinct sources of interference—eddy currents and secondary fields—are investigated under open-circuit and closed-circuit configurations, respectively. In each case, various strategies are proposed and implemented to decrease the interference. Their effectiveness is then experimentally validated through quantitative measurements, providing insight into practical methods for minimizing interference and improving overall system performance.

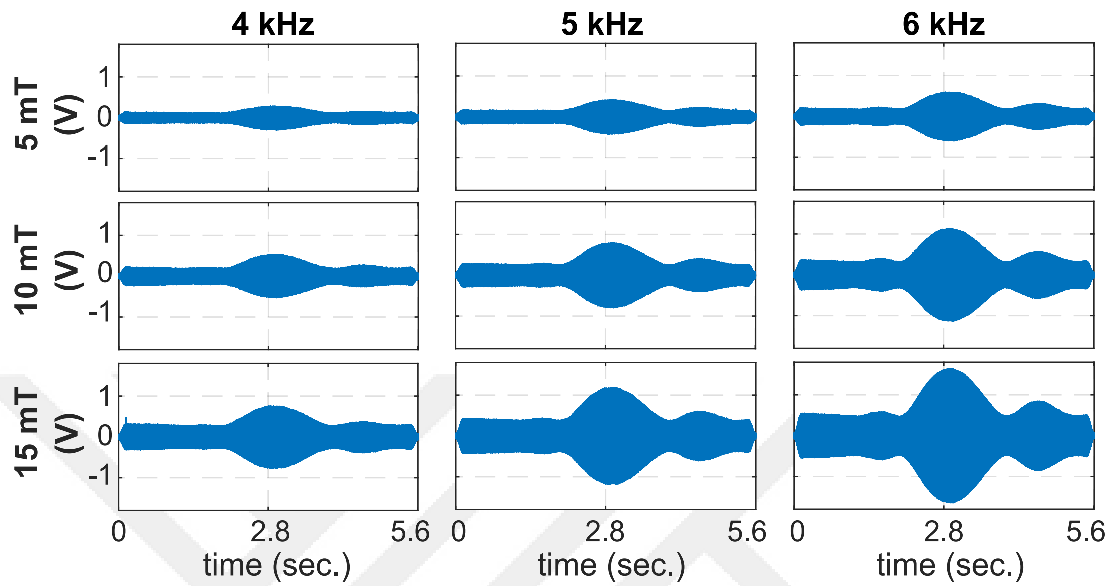

Figure 5.1: Effect of drive field frequency and amplitude on the interference signal observed at the receive coil due to eddy currents (ε_3). All experiments were conducted using a standard 4-layer copper wire saturation coil in open-circuit configuration. The drive field was applied at 4, 5, and 6 kHz with amplitudes of 5, 10, and 15 mT, respectively.

5.1.1 Eddy Currents: Experiment Results

To investigate the interference induced by the saturation coil in an MPI system, a series of interference experiments were conducted under two distinct electrical configurations: open-circuit and closed-circuit, as mentioned before. In the open-circuit configuration, the saturation coil was electrically disconnected from any power supply. This setup was used to isolate and examine interference mechanisms arising purely from eddy currents, particularly the ε_3 component.

Two sets of experiments were performed. In the first set, the DF amplitude (B_p) and DF frequency (f_d) were varied over 5, 10, and 15 mT, and 4, 5, and 6 kHz, respectively, to observe how these parameters influenced the induced interference on the receive coil as seen in Fig. 5.1.

To validate the analytical formulation derived for the eddy current-induced interference term ε_3, a comparison between simulated and experimental received

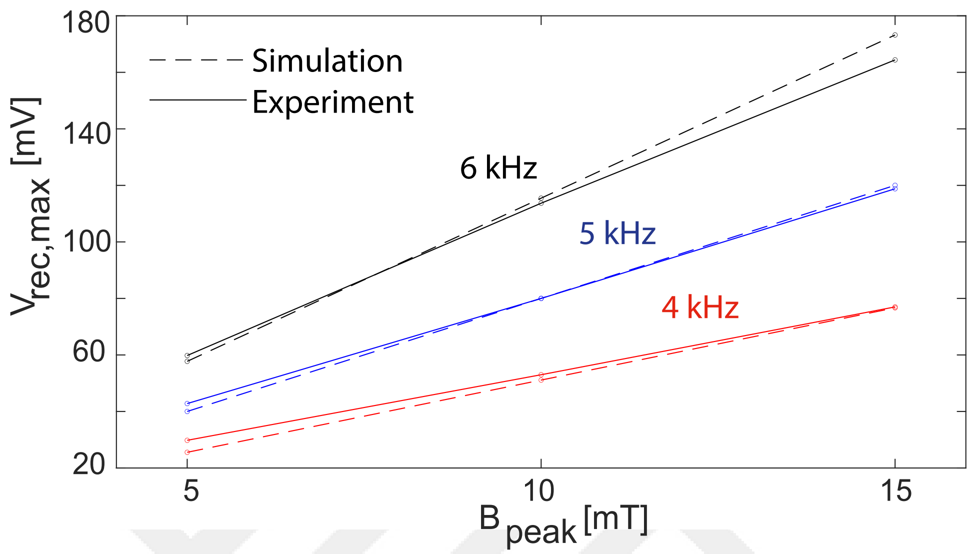

Figure 5.2: Comparison of experimental and simulated peak values of the interference signals caused by eddy currents (ε_3) in the open-circuit configuration.

signals was conducted. For the simulated signal, the theoretical model in Eq. 3.13 was utilized. Considering the geometry of the saturation coil and drive field parameters, Faraday's law of induction was utilized to predict the magnitude of the induced voltage in the receive coil.

As shown in Fig. 5.2, the simulation results based on this formulation exhibit excellent agreement with the experimentally measured peak values of the interference signal in the open-circuit configuration. This confirms that the interference mechanism in this configuration is accurately captured by the ε_3 term, thereby validating the use of the proposed model in Eq. 3.13 for predicting and mitigating eddy current effects in system design.

In the second set of experiments, the DF was fixed at 6 kHz and 10 mT, while the structural parameters of the saturation coil—such as number of layers and wire type—were systematically varied as seen in Fig. 5.3. The results validate that the increase in the number of windings and layers of the saturation coil results in an increase in ε_3. Figure 5.3 also compares the effects of using solid copper wire versus Litz wire for the saturation coil. The results show that using Litz wire prevents the formation of eddy currents, effectively diminishing ε_3.

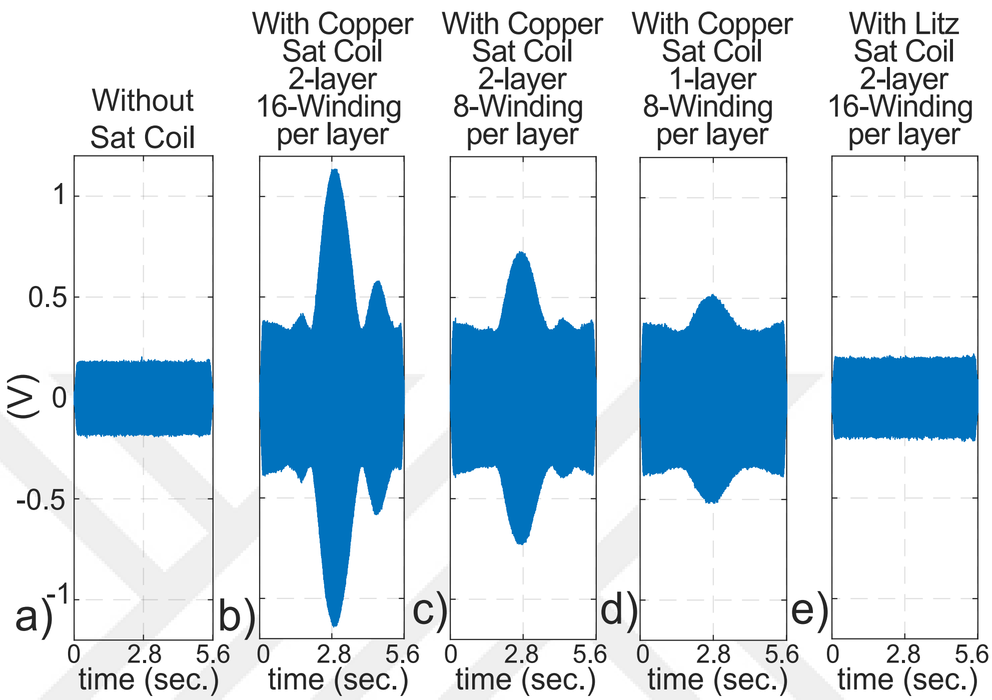

Figure 5.3: Saturation coils were tested in open-circuit configuration without the phantom to observe the effect of eddy currents (i.e., the contribution of ε_3). (a) No saturation coil. (b)–(d) Results for copper saturation coils with different layer and winding-per-layer configurations. (e) Result for the Litz wire saturation coil.

These experiments provided critical insights into the role of the saturation coil geometry and the type of wire in minimizing unintended electromagnetic coupling in the open-circuit scenario. For the remainder of the experiments, using a Litz wire is adopted as a solution to the interference problem originating from the eddy currents on the wires of the saturation coil.

5.1.2 Secondary Fields: Experiment Results

Figure 5.4 presents the experimental results of different approaches aimed at minimizing ε_2. It shows that when the saturation coil is directly connected to the DC current source, the LNA gain is limited to a maximum of 2. In contrast, in the absence of a saturation coil, the LNA gain can be increased up to 100. Depending on the concentration of MNPs, the received signal may be very weak

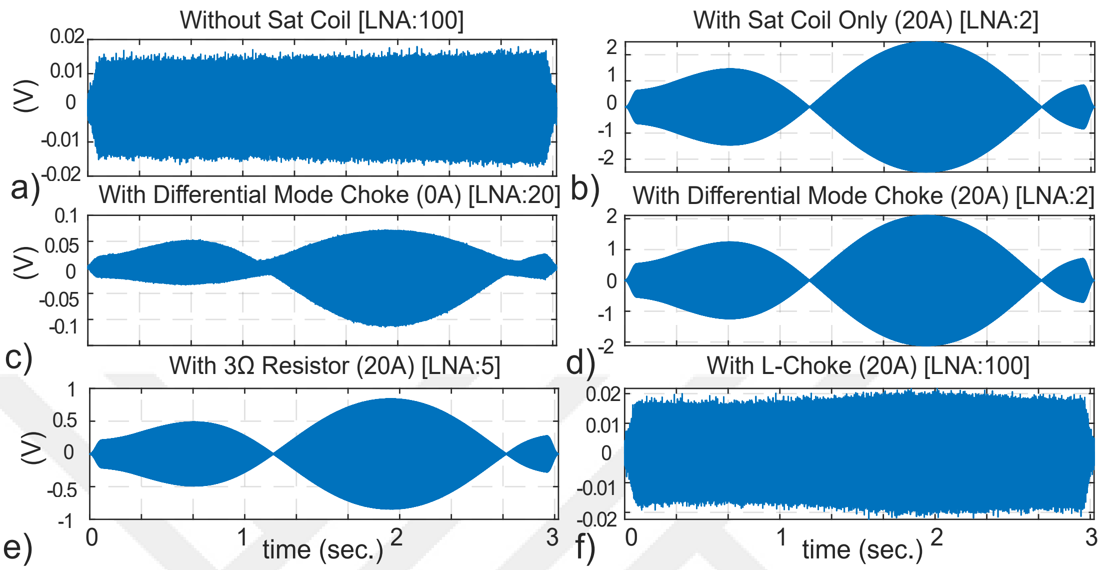

Figure 5.4: Investigation of interference due to secondary fields (ε_2) and potential strategies to prevent the secondary induction due to saturation coil. (a) No saturation coil. (b) Only the saturation coil is used with 20 A DC, leading to strong secondary induction on the receive coil. A differential mode choke (N:N turns) is connected in series with the saturation coil, with (c) 0 A DC and (d) 20 A DC through the saturation coil. (e) A 3 Ω resistor is connected in series with the saturation coil, with 20 A DC applied. (f) A large air-core L-choke is connected in series with the saturation coil, with 20 A DC applied.

and therefore requires high LNA gains. However, interference from the saturation coil limits the LNA gain to undesirably low values.

To address the interference due to secondary fields, a few different approaches were tested, with results shown in Fig 5.4. First, a N:N differential mode choke (with $N = 8$) was utilized, as illustrated in Fig. 4.3(c). In this approach, DC current does not encounter any large impedance and hence are not affected by the presence of the differential mode choke. On the other hand, AC currents induce opposing currents in the other winding, effectively canceling the currents responsible for interference. As shown in Fig. 5.4(c,d), the differential mode choke offers some improvement when DC current is not applied through the saturation coil, allowing the LNA gain to be increased to 20. However, when 20 A DC current is applied through the saturation coil, the magnetic permeability of the core decreases significantly, and the choke can no longer cancel the AC components effectively, as seen in Fig 5.4(d).

As described in Equation 3.13, ε_2 can be reduced by increasing the impedance seen by the saturation coil. However, the DC current source cannot deliver 20 A if the resistance exceeds 3 Ω at the DF frequency. Here, a 3 Ω resistor was connected in series with the saturation coil, as illustrated in Fig. 4.3(a). Figure 5.4(e) shows that this configuration only allows an LNA gain up to 5, which is insufficient for capturing the MNP signal.

Finally, we designed an L-choke with 27 mH inductance and 3 Ω resistance as shown in Fig. 4.3(a). This L-choke provides an impedance of approximately 2050 Ω at 12.1 kHz, while presenting only 3 Ω resistance to the DC current. Hence, the L-choke significantly increases the impedance in the ε_2 expression. Since the L-choke effectively reduces ε_2, Fig. 5.4(f) shows that it enables the LNA gain to be increased up to 100. Therefore, the L-choke is selected as the solution to the interference problem caused by the saturation coil in closed-circuit configuration.

5.2 Imaging Experiment Results

The experiments were conducted to evaluate the effectiveness of standard and improved saturation coils in selectively suppressing off-target signals while preserving the target region. The results are presented in two parts: 1D imaging results for a phantom with target and off-tagert regions seperated by 2.3 cm, and 2D imaging results for two different phantoms with 2.3 cm and 0.6 cm separations between the target and off-tagert regions.

5.2.1 1D Imaging Results

In the first step of the imaging experiments, the phantom with the off-target region positioned farther from the target region was utilized. During the imaging experiments, a 20 A DC current was applied, resulting in DC magnetic fields of approximately 52.6 mT and 27.8 mT over the off-target region when using the 4-layer and 2-layer saturation coils, respectively. Figure 5.5 confirms that, as expected, the 4-layer saturation coil generates a stronger DC magnetic field over the off-target region compared to the 2-layer coil, and it completely suppresses the off-target signal. However, as shown in Fig. 5.5, the middle target sample is also affected and partially saturated. To mitigate this issue, an improved saturation coil (4 layers, -3+20 windings per layer) was tested. Figure 5.5 demonstrates that the improved coil fully suppresses the off-target signal without affecting or saturating the middle target region. Therefore, the improved saturation coil design is adopted for more selective saturation, allowing suppression of the off-target region without compromising the target region.

5.2.2 2D Imaging Results

In the second step of the imaging experiments, both phantoms with 2.3 cm and 0.6 cm separations were used. For the phantom in which the off-target region was located farther from the target region, an improved saturation coil with -3+20 windings was used, whereas a -3+9 winding configuration was employed for the phantom with a closer off-target region. Figure 5.6 shows the performance of the improved saturation coil over phantoms with off-target regions located at different distances from the target region. The improved coil successfully saturates the off-target region in the phantom where it is far from the target, without affecting the target signal. However, when the off-target region is very close to the target, a sharper spatial selectivity is required. Achieving this would necessitate additional layers and reverse windings. Nonetheless, the scanner bore diameter limits the saturation coil to a maximum of 4 layers. Despite these restrictions, Fig. 5.6 indicates that the improved saturation coil with -3+9 windings is capable of distinguishing between very close target and off-target regions, even though it does not fully saturate the off-target region.

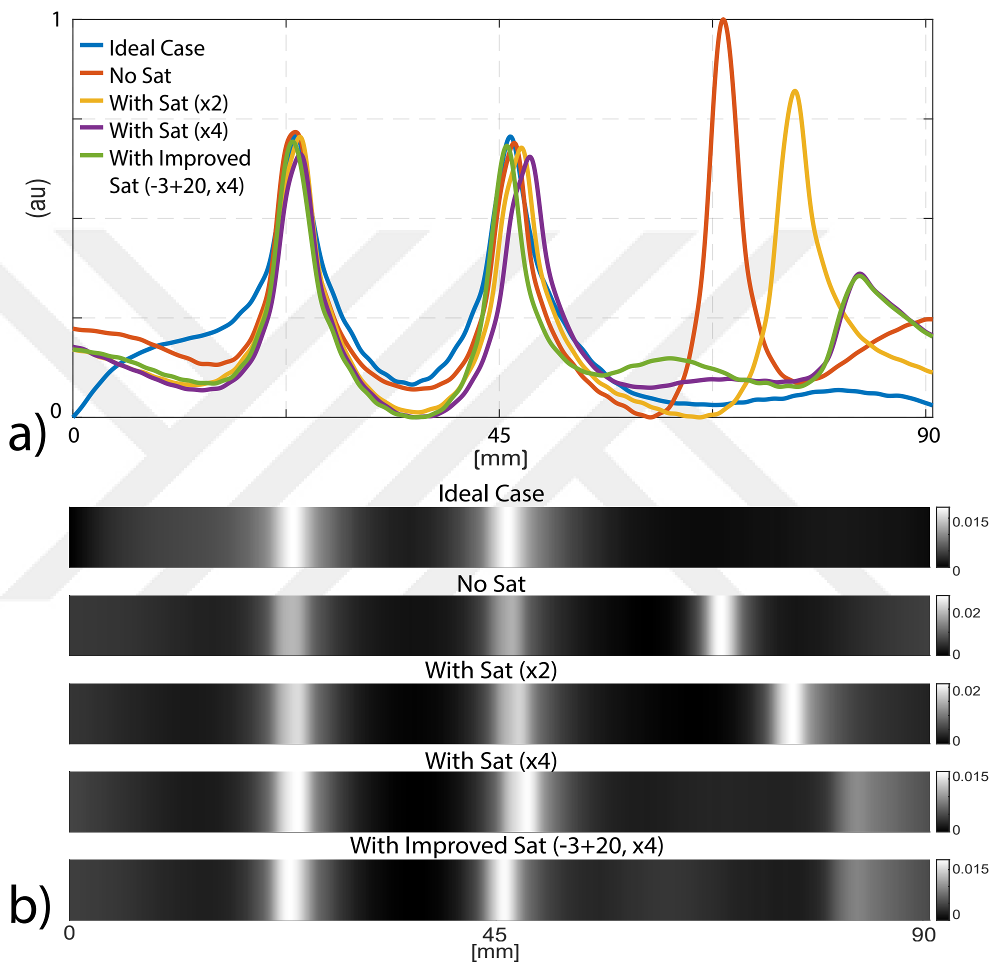

Figure 5.5: Results of 1D imaging experiments. (a) 1D cross-section images and (b) their stacked versions (in the vertical direction for display purposes) of a phantom with a 2.3 cm distance between the target and off-target regions. In the "Ideal Case", the off-target sample was removed from the phantom and only the target samples were included. The "No Sat" image shows the image of the full phantom including the target and off-target regions, but without any saturation coil. The effects of standard saturation coils with 2 and 4 layers (each driven with 20 A DC) are shown. The last image corresponds to an improved sat coil with 4 layers and -3+20 windings per layer, demonstrating effective suppression of the off-target signal while preserving the target region.

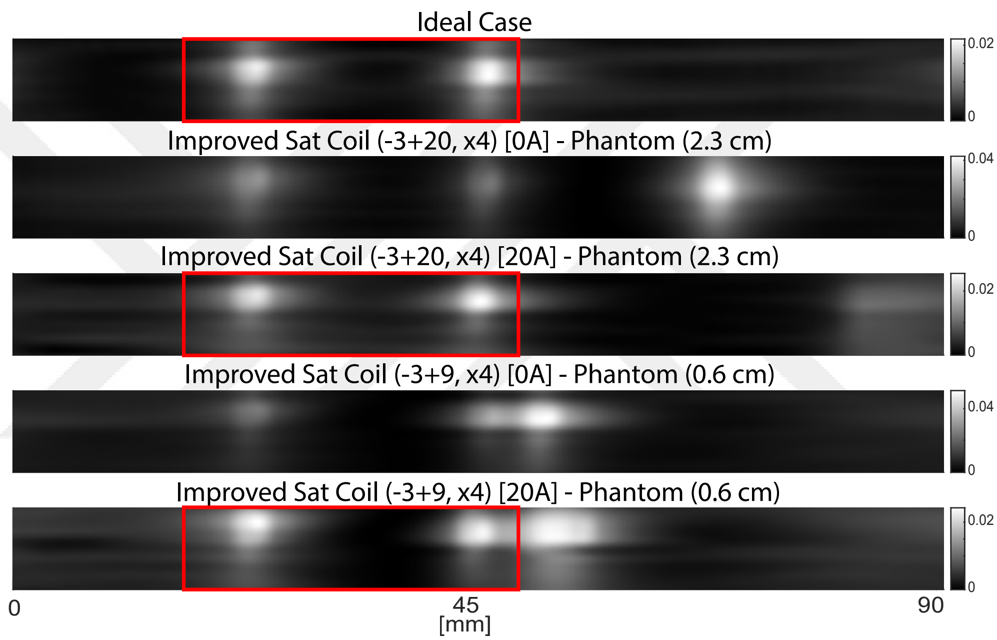

Figure 5.6: Results of 2D imaging experiments, demonstrating the performance of the improved saturation coils. In the "Ideal Case", the off-target sample was removed from the phantom and only the target samples were included. Subsequent images show results for phantoms with 2.3 cm and 0.6 cm spacing between target and off-target regions, with and without DC current applied to the saturation coils. The improved saturation coil with -3+20 windings completely suppressed the off-target region and preserved the target region when the off-target region was separated at 2.3 cm. Although the improved saturation coil with -3+9 windings did not fully suppress the off-target region separated at 0.6 cm, it successfully separated the intertwined target and off-target regions.

Chapter 6

Discussion and Conclusion

This thesis proposed a localized magnetic saturation approach to suppress unwanted signals from high-concentration off-target regions in MPI. As demonstrated via 1D and 2D imaging experiments, this technique effectively reduces the signal contribution of magnetically saturated areas. Because the integration of the saturation coil into the MPI scanner introduces interference signals on the receive chain of the MPI system, this thesis also proposes methods to overcome interference.

To address the interference problem, this thesis first formulated the total received signal analytically, as detailed in Equation. (3.12) and further elaborated in the Appendix. The analysis revealed two primary sources of interference caused by the saturation coil: $\varepsilon_2(t)$, caused by voltage coupling through the current path of the saturation coil, and $\varepsilon_3(t)$, caused by the eddy current induction in the saturation coil wire. Using a Litz wire instead of solid copper wire for winding the saturation coil effectively suppressed $\varepsilon_3(t)$, because the individually insulated small strands of the Litz wire minimizes eddy current formation by limiting circulating currents within the conductor. Moreover, incorporating a large-inductance L-choke in series with the saturation coil significantly attenuated $\varepsilon_2(t)$ by creating a large impedance at the DF frequency.

As an alternative interference mitigation strategy, a differential-mode choke was tested based on an N:N reversed-wound transformer connected in series with the saturation coil. While this method successfully eliminated coupling in the absence of a DC current, under the operational condition of 20 A DC current, the magnetic permeability of the iron core deteriorated substantially. As a result, the differential mode choke became ineffective at blocking the interference, as depicted in Fig. 5.4(c,d). Given the need for a relatively strong DC magnetic field to achieve effective local saturation (on the order of 20 A for the experimental results in this thesis), using a differential-mode choke was deemed unsuitable.

In contrast, the air-core L-choke used in this study remains unaffected by high DC currents, since it does not rely on a magnetic core and thus its inductance remains stable. To achieve a sufficiently high inductance value (e.g., 27 mH in this thesis) for effective suppression of interference at DF frequency, a large number of windings was required due to the absence of magnetic material.

An alternative method to eliminate $\varepsilon_2(t)$ involves using a parallel LC circuit in series with the saturation coil. If the resonance frequency of this parallel LC circuit is tuned to the DF frequency, it can present a high impedance in the current path of the saturation coil, thereby attenuating the coupled interference. However, similar to the L-choke solution, the inductor in this LC circuit needs to be an air core inductor. If a magnetic core is utilized, the inductance value can significantly vary due to magnetic saturation effects, which in turn can shift the resonance frequency of the LC circuit and reduce the impedance at the desired frequency.

Nevertheless, there exist magnetic materials whose permeability characteristics change predictably under high DC bias [35]. These materials may offer a promising direction for future designs of parallel LC circuits or differential-mode chokes that can maintain performance in the presence of strong DC currents, potentially enabling more compact or efficient interference suppression solutions.

Following the resolution of the interference issues, 1D imaging experiments were performed to evaluate the efficacy of saturation coils. In our initial experiments, a coil that generated approximately 52 mT at the location of the off-target region showed promising results. Given the 4.4 T/m gradient strength of the MPI system, this field was nearly sufficient to fully saturate the MNPs in the off-target zone. However, as illustrated in Fig. 5.5(b), the strong magnetic field also slightly affected the central target sample, indicating limited spatial selectivity under these constraints. To address this limitation, an improved saturation coil design that incorporated reverse windings was proposed and tested. This configuration significantly improved spatial selectivity by generating a sharper magnetic field profile that effectively saturated the off-target region while minimizing the field extending into the adjacent target areas.

Subsequently, 2D imaging experiments were conducted. Due to the high SF gradient of 4.4 T/m along the z-axis, our FFL MPI scanner exhibits high spatial resolution and is therefore highly sensitive to even minor positional deviations. During the course of the experiments, both the phantoms and the saturation coils were repositioned between scans. Consequently, small shifts in object placement resulted in slight misalignments in the reconstructed 2D images, making it more difficult to quantitatively compare signal intensities across different scans.

Additionally, 2D imaging experiments were conducted using a phantom in which the off-target region was located closer to the target region. Despite the small separation and the resulting intertwining between the off-target and target regions, the central target sample remained partially distinguishable, primarily due to the high SF gradient. The high SF gradient of our FFL MPI scanner also made it challenging to demonstrate the problem and the benefits of the improved saturation coil. Nonetheless, the use of an improved coil improved spatial separation, with the resulting MPI image closely resembling the ideal case.

To further optimize the spatial selectivity in 2D imaging, improved coils with different winding configurations were evaluated. The experimental results demonstrate that local saturation using improved coils incorporating reverse windings is a promising approach for selective signal suppression in MPI, even for MPI systems with high-gradient SFs.

In this thesis, hardware limitations restricted the DC current of the saturation coil. Additionally, physical constraints, such as the bore diameter of the MPI scanner, restricted the number of layers on the saturation coil. Consequently, for the experiments in this thesis, the saturation coil was limited to a maximum of 4 layers, with a maximum of 20 A DC current. In the case of a larger bore MPI scanner, alternative coil designs can be explored to achieve better confinement of the saturation field. Optimizing the coil geometry and winding configurations can create sharper and more localized saturation regions, leading to precise suppression of signals from off-target regions in MPI without compromising the integrity of signals from the target regions.

In this thesis, the phantom and the saturation coil were moved inside the MPI scanner during imaging, as our FFL MPI scanner does not utilize FFs. For a system that incorporates FFs for moving the FFR, the speed v of the saturation coil in Eq (3.13) would be zero. In the interference relations given in Eq (3.13), the effect of speed is to impose a time-varying amplitude to the interference signals. In the absence of movement, both the saturation coil and the phantom would remain stationary, and the entire system would be static. Therefore, the interference signals would still be present, albeit with constant amplitude. Therefore, the solutions proposed in this thesis to mitigate interference signals would still be needed and applicable in such a case. Additionally, introducing extra coils that generate FFs may also induce eddy currents and inductions in the system. Similar approaches of preventing eddy currents on the FF coil wires and current through the FF coils can also be employed to overcome these issues.

In conclusion, this thesis proposed using a saturation coil to suppress the signal from high-concentration off-target regions, and presented methods for overcoming the interference signals due to the saturation coil. The experimental results showed that the saturation coil successfully suppressed the off-target region when it is away from the target region, and successfully separated the target and off-target regions when they were close to each other with their signals intertwined.

Bibliography

[1] B. Gleich and J. Weizenecker, "Tomographic imaging using the nonlinear response of magnetic particles," *Nature*, vol. 435, pp. 1214–1217, Jun 2005.

[2] P. W. Goodwill, J. J. Konkle, B. Zheng, E. U. Saritas, and S. M. Conolly, "Projection x-space magnetic particle imaging," *IEEE Transactions on Medical Imaging*, vol. 31, no. 5, pp. 1076–1085, 2012.

[3] E. U. Saritas, P. W. Goodwill, G. Z. Zhang, and S. M. Conolly, "Magnetostimulation limits in magnetic particle imaging," *IEEE Transactions on Medical Imaging*, vol. 32, no. 9, pp. 1600–1610, 2013.

[4] I. Molwitz *et al.*, "First magnetic particle imaging angiography in human-sized organs by employing a multimodal ex vivo pig kidney perfusion system," *Physiological Measurement*, vol. 40, no. 10, 2019.

[5] K. Them *et al.*, "Increasing the sensitivity for stem cell monitoring in system-function based magnetic particle imaging," *Physics in Medicine Biology*, vol. 61, no. 9, pp. 3279–3290, 2016.

[6] Q. Wang *et al.*, "Artificially engineered cubic iron oxide nanoparticle as a high-performance magnetic particle imaging tracer for stem cell tracking," *ACS Nano*, vol. 14, no. 2, pp. 2053–2062, 2020.

[7] D. B. Mangarova *et al.*, "Ex vivo magnetic particle imaging of vascular inflammation in abdominal aortic aneurysm in a murine model," *Scientific Reports*, vol. 10, no. 1, p. 12410, 2020.

[8] P. Chandrasekharan *et al.*, "Non-radioactive and sensitive tracking of neutrophils towards inflammation using antibody functionalized magnetic particle imaging tracers," *Nanotheranostics*, vol. 5, no. 2, pp. 240–255, 2021.

[9] X. Zhu *et al.*, "Quantitative drug release monitoring in tumors of living subjects by magnetic particle imaging nanocomposite," *Nano Letters*, vol. 19, no. 10, pp. 6725–6733, 2019.

[10] Z. W. Tay *et al.*, "In vivo tracking and quantification of inhaled aerosol using magnetic particle imaging towards inhaled therapeutic monitoring," *Theranostics*, vol. 8, no. 13, pp. 3676–3687, 2018.

[11] R. Orendorff *et al.*, "First in vivo traumatic brain injury imaging via magnetic particle imaging," *Physics in Medicine Biology*, vol. 62, no. 9, pp. 3501–3509, 2017.

[12] E. Y. Yu *et al.*, "Magnetic particle imaging: A novel in vivo imaging platform for cancer detection," *Nano Letters*, vol. 17, no. 3, pp. 1648–1654, 2017.

[13] Z. W. Tay *et al.*, "Magnetic particle imaging-guided heating in vivo using gradient fields for arbitrary localization of magnetic hyperthermia therapy," *ACS Nano*, vol. 12, no. 4, pp. 3699–3713, 2018.

[14] L. C. Wu *et al.*, "A review of magnetic particle imaging and perspectives on neuroimaging," *American Journal of Neuroradiology*, vol. 40, pp. 206–212, Feb 2019.

[15] B. Zheng, E. W. Lo, P. W. Goodwill, and S. M. Conolly, "Optimal broadband noise matching to inductive sensors: Application to magnetic particle imaging," *IEEE Transactions on Biomedical Circuits and Systems*, vol. 11, no. 5, pp. 1041–1052, 2017.

[16] P. W. Goodwill and S. M. Conolly, "The x-space formulation of the magnetic particle imaging process: 1-d signal, resolution, bandwidth, snr, sar, and magnetostimulation," *IEEE Transactions on Medical Imaging*, vol. 29, no. 11, pp. 1851–1859, 2010.

[17] T. Knopp and T. M. Buzug, *Magnetic Particle Imaging: An Introduction to Imaging Principles and Scanner Instrumentation*. Springer Science & Business Media, 2012.

[18] P. Goodwill, L. Croft, J. Konkle, K. Lu, E. Saritas, B. Zheng, and S. Conolly, "Third generation x-space mpi mouse and rat scanner," in *Magnetic Particle Imaging: A Novel SPIO Nanoparticle Imaging Technique*, pp. 261–265, Springer, 2012.

[19] P. W. Goodwill, L. R. Croft, J. J. Konkle, K. Lu, E. U. Saritas, B. Zheng, and S. M. Conolly, "A 7 t/m 3d x-space mpi mouse and rat scanner," in *2013 International Workshop on Magnetic Particle Imaging (IWMPI)*, pp. 1–1, IEEE, 2013.

[20] P. W. Goodwill and S. M. Conolly, "Multidimensional x-space magnetic particle imaging," *IEEE Transactions on Medical Imaging*, vol. 30, no. 9, pp. 1581–1590, 2011. Epub 2011 Mar 10.

[21] T. M. Buzug, G. Bringout, M. Erbe, K. Gräfe, M. Graeser, M. Grüttner, A. Halkola, T. F. Sattel, W. Tenner, H. Wojtczyk, *et al.*, "Magnetic particle imaging: Introduction to imaging and hardware realization," *Zeitschrift für Medizinische Physik*, vol. 22, no. 4, pp. 323–334, 2012.

[22] A. R. Cagıl and E. U. Saritas, "Design of a preclinical field free point/field free line hybrid mpi scanner," in *Proceedings of the International Workshop on Magnetic Particle Imaging (IWMPI)*, 2019.

[23] M. Ütkür, Y. Muslu, and E. Ülkü Sarıtaş, "A 4.8 t/m magnetic particle imaging scanner design and construction," in *2017 21st National Biomedical Engineering Meeting (BIYOMUT)*, IEEE, 2017. Conference paper.

[24] A. R. Çağıl, "A novel preclinical dual-topology magnetic particle imaging scanner," master's thesis, Bilkent University, December 2020.

[25] N. Panagiotopoulos, R. L. Duschka, M. Ahlborg, G. Bringout, C. Debbeler, M. Graeser, C. Kaethner, K. Lüdtke-Buzug, H. Medimagh, J. Stelzner, *et al.*, "Magnetic particle imaging: Current developments and future directions," *International Journal of Nanomedicine*, pp. 3097–3114, 2015.

[26] Z. W. Tay, D. Hensley, J. Ma, P. Chandrasekharan, B. Zheng, P. Goodwill, and S. Conolly, "Pulsed excitation in magnetic particle imaging," *IEEE Transactions on Medical Imaging*, vol. 38, no. 10, pp. 2389–2399, 2019.

[27] "LFR Current Probe." http://www.pemuk.com/products/lfr-currentprobe.aspx.

[28] M. Graeser, T. Knopp, P. Szwargulski, T. Friedrich, A. V. Gladiß, M. Kaul, K. M. Krishnan, H. Ittrich, G. Adam, and T. M. Buzug, "Towards picogram detection of superparamagnetic iron-oxide particles using a gradiometric receive coil," *Scientific Reports*, vol. 7, no. 1, p. 6872, 2017.

[29] M. Utkur and E. U. Saritas, "Comparison of different coil topologies for an mpi relaxometer," in *2015 5th International Workshop on Magnetic Particle Imaging (IWMPI)*, 2015.

[30] P. Karp and D. Duret, "Unidirectional magnetic gradiometers," *Journal of Applied Physics*, vol. 51, no. 3, pp. 1267–1272, 1980.

[31] Z. W. Tay, A. Chandrasekharan, P. W. Goodwill, and S. M. Conolly, "A high-throughput, arbitrary-waveform, mpi spectrometer and relaxometer for comprehensive magnetic particle optimization and characterization," *Scientific Reports*, vol. 6, p. 34180, 2016.

[32] S. Kurt, Y. Muslu, and E. U. Saritas, "Partial fov center imaging (pci): A robust x-space image reconstruction for magnetic particle imaging," *IEEE Transactions on Medical Imaging*, vol. 39, no. 11, pp. 3441–3450, 2020.

[33] E. P. Furlani, *Permanent Magnet and Electromechanical Devices: Materials, Analysis, and Applications.* Academic Press, 2001.

[34] B. Alyuz, M. T. Arslan, M. Utkur, and E. U. Saritas, "Single-pass relaxation mapping at multiple frequencies using an arbitrary waveform mpi scanner," *International Journal on Magnetic Particle Imaging (IJMPI)*, vol. 9, no. 1 Suppl 1, p. –, 2023. Published Mar 19, 2023; Scopus-indexed.

[35] X. Cui, J. Zhou, J. Pang, K. Qiu, X. Li, J. You, D. Yang, and J. Bu, "Achieving constant magnetic permeability in fe-based nanocrystalline alloys

by ni alloying and magnetic-field annealing for high dc bias capability and low coercivity," *Journal of Applied Physics*, vol. 136, p. 135103, 10 2024.

Appendix A

Mathematical Characterization of Baseline Signal

A typical MPI scanner incorporates selection field, drive, and receive coils. Typically, a copper shield is also placed between the selection field and drive coils to prevent induced voltages and currents on the selection field coils. In our derivations below, due to the presence of the copper shield, we ignore the effects of the selection field coils on the received signal. Without loss of generality, we assume that the drive field is homogeneous and is given as $B_d(t) = B_p sin(\omega t)$. We also assume that the saturation coil moves inside the receive chamber together with the phantom, at a constant velocity, v, in the z-direction.

If the drive field is considered as not homogeneous, it is given as $B_d(x, y, z, t) = B_p(x, y, z)sin(\omega t)$. Because the saturation coil is also moving inside the drive field, the position dependent term of $B_p(x, y, z)$ has a time dependent effect on the induced voltage over the receive coil, which results in an additional time derivative term. On the other hand, by considering the velocity is much less than the frequency, this term can be ignored. Although time derivative term is ignored, there is still $B_p(x, y, z)$ term which is directly proportional to the induced voltage over the receive coil with respect to the position of the saturation coil.

Under these circumstances, the baseline voltage on the receive coil can be expressed as a superposition of three components as given in Equation. (3.12). These voltages are derived below using Faraday's law of induction.

A.1 Direct Feedthrough Voltage

To minimize the direct feedthrough interference between the drive and receive coils, the receive coil is typically wound in a gradiometric fashion, as depicted in Figure 4.2. Then, the total linkage flux over the receive coil due to the drive field can be expressed as:

$$\phi_1(t) = \sum_{i=1}^{N_r} W_{r,i} \iint_{A_r} B_d(t)dxdy = A_r B_p sin(wt) \sum_{i=1}^{N_r} W_{r,i} \tag{A.1}$$

where A_r is the axial cross-sectional area, N_r is the total number of windings, and $W_{r,i} = \pm 1$ is the winding sense of the i^{th} winding of the gradiometric receive coil. Then, the direct feedthrough voltage can be expressed as:

$$\varepsilon_1(t) = -\frac{d\phi_1(t)}{dt} = -A_r B_p \omega cos(\omega t) \sum_{i=1}^{N_r} W_{r,i} \tag{A.2}$$

A.2 Voltage Due to Secondary Fields Created by Saturation Coil

The drive field induces voltage on the saturation, which in turn causes secondary fields that induce a voltage on the receive coil. Firstly, the total linkage flux on the saturation coil can be expressed as:

$$\phi_s(t) = \sum_{i=1}^{N_s} \iint_{A_s} B_d(t)dxdy = A_s N_s B_p sin(wt) \tag{A.3}$$

where N_s is the total number of and A_s is the axial cross-sectional area of the saturation coil. Then, the voltage induced on the saturation coil is:

$$\varepsilon_s(t) = -\frac{d\phi_s(t)}{dt} = -A_s N_s B_p \omega cos(\omega t) \tag{A.4}$$

If the impedance of the overall circuit (i.e., the impedance of the saturation coil in series with the impedance seen by the saturation coil) is $Z_s = |Z_s|e^{j\theta_s}$, the current over the saturation coil can be expressed as:

$$i_s(t) = -A_s N_s B_p \frac{\omega}{|Z_s|} cos(\omega t - \theta_s) \tag{A.5}$$

Let $S_s(x, y, z)$ be the coil efficiency map (i.e., field per unit current through the coil) of the saturation coil along the z-direction. Then, considering the linear movement of the saturation coil, the B-field along the z-direction due to the current $i_s(t)$ is $B_s(x, y, z, t) = S_s(x, y, z - vt)i_s(t)$. This secondary field due to the saturation coil creates a linkage flux over the receive coil, which can be expressed as follows:

$$\begin{aligned}
\phi_2(t) =& \sum_{i=1}^{N_r} W_{r,i} \iint_{A_r} B_s(x, y, z_{r,i}, t) dxdy \\
=& - A_s N_s B_p \frac{\omega}{|Z_s|} cos(\omega t - \theta_s) \\
& \times \sum_{i=1}^{N_r} W_{r,i} \iint_{A_r} S_s(x, y, z_{r,i} - vt) dxdy
\end{aligned} \tag{A.6}$$

where $z_{r,i}$ is the z-axis position of the i^{th} receive coil winding. Finally, the induced voltage on the receive coil can be expressed as:

$$\begin{aligned}
\varepsilon_2(t) =& -\frac{d\phi_2(t)}{dt} \\
=& - A_s N_s B_p \frac{\omega^2}{|Z_s|} sin(\omega t - \theta_s) \\
& \times \sum_{i=1}^{N_r} W_{r,i} \iint_{A_r} S_s(x, y, z_{r,i} - vt) dxdy \\
& - A_s N_s B_p \frac{\omega}{|Z_s|} vcos(\omega t - \theta_s) \\
& \times \sum_{i=1}^{N_r} W_{r,i} \iint_{A_r} \left. \frac{dS_s(x, y, z)}{dz} \right|_{z=z_{r,i}-vt} dxdy
\end{aligned} \tag{A.7}$$

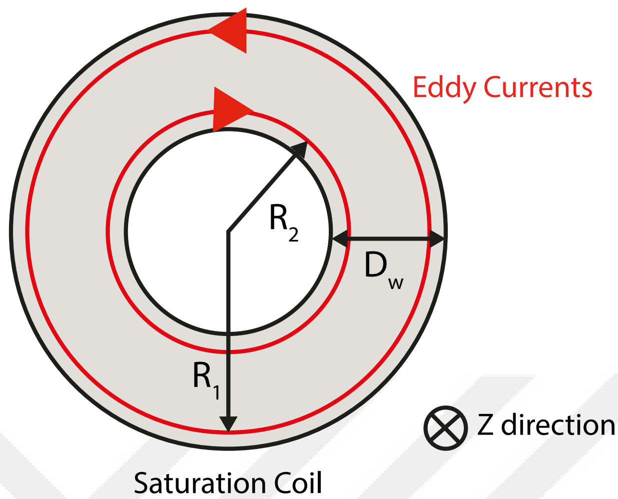

Figure A.1: Conceptual diagram of cross-sectional view of a copper saturation coil illustrating the formation of eddy currents within the windings. The diagram conceptually represents the source of interference (ε_3) in the open-circuit configuration.

Here, the second term is due to the speed v at which the saturation coil is moved. Assuming that the speed of movement is in the range of cm/sec and the drive field frequency is in the range of kHz, the second term is approximately 4 orders of magnitude smaller than the first term (based on simulation results not shown), and hence can be ignored. Hence, the induced voltage due to the secondary field created by the saturation coil can be approximated as:

$$\begin{aligned}\varepsilon_2(t) \approx & - A_s N_s B_p \frac{\omega^2}{|Z_s|} sin(\omega t - \theta_s) \\ & \times \sum_{i=1}^{N_r} W_{r,i} \iint_{A_r} S_s(x, y, z_{r,i} - vt) dx dy\end{aligned} \tag{A.8}$$

Note that for an infinitely long solenoidal receive coil with $W_{r,i} = 1$ for all windings, the integral term would yield a constant value independent of t. In the case of a finite-length gradiometric receive coil, the second term causes the magnitude of the induced voltage to change with t.

A.3 Voltage Due to Eddy Currents on Saturation Coil

The eddy currents inside the copper wires of the saturation coil also create secondary fields over the receive coil. As depicted in Fig. A.1, the effective eddy currents can be approximated as flowing on the outer and the inner surfaces of the wire, each of which will create a magnetic field that induces a voltage on the receive coil.

Let us first consider a solid copper disc of radius R and thickness D. When exposed to B-field $B_d(t)$, the eddy currents will flow only in a region close to the outer surface of this disc. The magnetic flux in the copper cross-section of the disc in xy-plane can be expressed as:

$$\phi_e(t) = \iint_{A_R} B_d(t)dxdy = \pi R^2 B_p sin(\omega t) \tag{A.9}$$

Then, the voltage induced on the disc is:

$$\varepsilon_e(t) = -\frac{d\phi_e(t)}{dt} = -\pi R^2 B_p \omega cos(\omega t) \tag{A.10}$$

If the impedance along the circular path of the eddy current is $Z = |Z|e^{j\theta}$, this voltage creates an eddy current that can be written as:

$$i_e(t) = -\pi R^2 B_p \frac{\omega}{|Z|} cos(\omega t - \theta) \tag{A.11}$$

Considering a cylindrical structure that consists of N such solid copper discs placed along the z-axis, each disc would have an eddy current $i_R(t)$ along its outer surface when exposed to $B_d(t)$. Let $S_R(x, y, z)$ be the coil efficiency map (i.e., field per unit current) for the cylindrical structure with radius R. Then, considering the linear movement of the discs, the B-field along the z-direction due to the current $i_e(t)$ is $B_e(x, y, z, t) = S_R(x, y, z - vt)i_e(t)$. This secondary field creates a linkage flux over the receive coil, which can be expressed as follows:

$$
\begin{aligned}
\phi_R(t) =& \sum_{i=1}^{N_r} W_{r,i} \iint_{A_r} B_e(x, y, z_{r,i}, t)dxdy \\
=& -\pi R^2 B_p \frac{\omega}{|Z|} cos(\omega t - \theta) \\
& \times \sum_{i=1}^{N_r} W_{r,i} \iint_{A_r} S_R(x, y, z_{r,i} - vt)dxdy
\end{aligned}
\tag{A.12}
$$

Next, we model the saturation coil as the difference of two cylindrical structures of radii R_o and R_{in}, where R_o and R_{in} are the outer and inner radii of the saturation coil, respectively. In this model, each cylindrical structure is composed of $N = N_s$ discs, with thickness $D = D_w$ equal to the diameter of the wire used for winding the saturation coil. Note that $R_o = R_{in} + D_w$ for a single layer saturation coil. Then, as depicted in Fig. A.1, the effective eddy currents flowing on the outer and the inner surfaces of the wire will be in reverse direction, creating a linkage flux that can be written as:

$$
\begin{aligned}
\phi_3(t) =& \phi_{R_o}(t) - \phi_{R_{in}}(t) \\
=& -\pi R_o^2 B_p \frac{\omega}{|Z_o|} cos(\omega t - \theta_o) \\
& \times \sum_{i=1}^{N_r} W_{r,i} \iint_{A_r} S_{R_o}(x, y, z_{r,i} - vt)dxdy \\
& + \pi R_{in}^2 B_p \frac{\omega}{|Z_{in}|} cos(\omega t - \theta_{in}) \\
& \times \sum_{i=1}^{N_r} W_{r,i} \iint_{A_r} S_{R_{in}}(x, y, z_{r,i} - vt)dxdy
\end{aligned}
\tag{A.13}
$$

If R_o is suffiently larger than D_w, we can assume that $S_s(x, y, z) \approx S_{R_o}(x, y, z) \approx S_{R_{in}}(x, y, z)$, where $S_s(x, y, z)$ is the coil efficiency map of the saturation coil as before. Then,

$$
\begin{aligned}
\phi_3(t) =& -\pi B_p \omega \left(\frac{R_o^2}{|Z_o|} cos(\omega t - \theta_o) - \frac{R_{in}^2}{|Z_{in}|} cos(\omega t - \theta_{in}) \right) \\
& \times \sum_{i=1}^{N_r} W_{r,i} \iint_{A_r} S_s(x, y, z_{r,i} - vt)dxdy
\end{aligned}
\tag{A.14}
$$

Finally, the induced voltage on the receive coil can be expressed as:

$$\begin{aligned}
\varepsilon_3(t) =& -\frac{d\phi_3(t)}{dt} \\
=& -\pi B_p \omega^2 \left(\frac{R_o^2}{|Z_o|} sin(\omega t - \theta_o) - \frac{R_{in}^2}{|Z_{in}|} sin(\omega t - \theta_{in}) \right) \\
& \times \sum_{i=1}^{N_r} W_{r,i} \iint_{A_r} S_s(x, y, z_{r,i} - vt) dxdy \\
& - \pi B_p \omega v \left(\frac{R_o^2}{|Z_o|} cos(\omega t - \theta_o) - \frac{R_{in}^2}{|Z_{in}|} cos(\omega t - \theta_{in}) \right) \\
& \times \sum_{i=1}^{N_r} W_{r,i} \iint_{A_r} \left. \frac{dS_s(x, y, z)}{dz} \right|_{z = z_{r,i} - vt} dxdy
\end{aligned} \tag{A.15}$$

Similar to the case in Eq. (A.7), the second term is due to the speed v at which the saturation coil is moved and is significantly smaller than the first term. Therefore, the induced voltage due to the eddy currents on the saturation coil can be approximated as:

$$\begin{aligned}
\varepsilon_3(t) \approx& -\pi B_p \omega^2 \left(\frac{R_o^2}{|Z_o|} sin(\omega t - \theta_o) - \frac{R_{in}^2}{|Z_{in}|} sin(\omega t - \theta_{in}) \right) \\
& \times \sum_{i=1}^{N_r} W_{r,i} \iint_{A_r} S_s(x, y, z_{r,i} - vt) dxdy
\end{aligned} \tag{A.16}$$